A Linear Theory of Extratropical Synoptic Eddy Statistics

JEFFREY S. WHITAKER AND PRASHANT D. SARDESHMUKH

Cooperative Institute for Research in the Environmental Sciences, University of Colorado, Boulder, Colorado

(Manuscript received 3 May 1996, in final form 27 May 1997)

ABSTRACT

This paper investigates the extent to which the statistics of extratropical synoptic eddies may be deduced from the assumption that the eddies are stochastically forced disturbances evolving on a baroclinically *stable* background flow. To this end, a two-level hemispheric quasigeostrophic model is linearized about the observed long-term mean flow and forced with Gaussian white noise. The mean flow is baroclinically stable for a reasonable choice of dissipation parameters. Synoptic-scale eddy disturbances can still grow on such a flow, albeit for a finite time, either in response to the stochastic forcing or through baroclinic and barotropic energy interactions with the background flow. In a statistically steady state, a fluctuation–dissipation relation (FDR) links the covariance of the eddies to the spatial structure of the background flow and the covariance of the forcing. Although not necessary, in this study the forcing is assumed to have always the same trivial statistics (white in both space and time). Under this assumption, the FDR states that the geographical distribution of synoptic eddy covariance is controlled solely by the spatial structure of the background flow, which can therefore be used to predict it. All other second-order eddy statistics, such as eddy kinetic energy, momentum and heat fluxes, and power spectra, can then also be predicted. Despite the apparently drastic underlying assumption of synoptic eddy evolution as a stable linear Markov process, the comparisons of the predicted and observed geographical distributions of eddy kinetic energy and momentum and heat fluxes are found to be encouraging. The FDR is also shown to be sensitive enough to basic-state changes that it is able to predict important aspects of observed storm-track variability associated with seasonal and interannual changes of the background flow. The success of these calculations suggests that it is not necessary to invoke either baroclinic instability or the details of the eddy forcing to understand much of the observed spatial and temporal structure of extratropical synoptic eddy statistics. Rather, the dynamics of nonmodal eddy growth in the Pacific and Atlantic jets, and the downstream propagation and dispersion of the eddy activity in the diffluent regions downstream of the jets, appear sufficient for this purpose.

1. Introduction

The last two decades have seen considerable progress in the modeling and prediction of extratropical weather systems. Numerical weather prediction models are now able to forecast them up to nearly a week ahead of time, and many general circulation models (GCMs) are able to capture important aspects of their general behavior as represented in the variance and covariance statistics of transient fluctuations with periods of less than about a week. Parallel advances have also been made in the understanding of their dynamics in a variety of situations, aided in significant measure by ''potential vorticity thinking.''

Despite these advances, however, a successful theory of the *statistics* of such eddies has yet to emerge. By itself, a reasonable simulation of the eddy statistics in GCMs does not constitute such a theory. Without a theory one cannot understand why, for example, a GCM produces synoptic eddy variance maxima where it does, or why it does not produce variance maxima where it should. A quantitative theory of the eddy statistics would help one understand such model deficiencies. It would also help one understand better the geographical distributions of the observed climatological mean synoptic eddy variances and fluxes, as well as their changes from season to season, from year to year, and during persistent extreme anomaly events.

Synoptic eddies have almost always been discussed in relation to a background flow, either steady, time-mean, slowly evolving, or representative of some ''instantaneous'' weather regime. When the focus shifts from the behavior of individual eddies to that of an ensemble of eddies, consideration of the ensemble-average flow as a background flow seems even more relevant. Nevertheless, as is well recognized, such a separation of the flow into mean and eddy parts often presents conceptual difficulties, and also raises the issue of whether, and to what extent, the mean flow actually *determines* the eddy statistics or vice versa. Still, one can always ask the question: Given an ensemble-average flow, to what extent can one deduce the ensemble-av-

Corresponding author address: Dr. Jeffrey S. Whitaker, CIRES, University of Colorado, Campus Box 449, Boulder, CO 80309-0449. E-mail: jsw@cdc.noaa.gov

erage eddy statistics? This is the problem considered in this paper.

The association of the geographical distribution of synoptic eddy variance with the spatial structure of the background flow has long been appreciated in the literature. Blackmon et al. (1977) noted that the climatological synoptic eddy variance maxima during northern winter are located just downstream of the climatological Pacific and Atlantic jets. Lau (1988) and Metz (1989) showed that slow monthly variations of the eddy statistics are also significantly correlated with slow variations of the background flow. Frederiksen (1983, 1989) and Robertson and Metz (1989, 1990) showed that some of these observational features can be related to the structures of the most unstable eigenmodes of the zonally varying climatological flow and how those structures change with changes in the background flow.

One could certainly formulate a theory of synoptic eddy statistics in terms of the fastest growing eigenmodes of the background flow. There are, however, several reasons why one might wish to avoid such a theory. First, the most unstable modes of observed zonally varying flows are often not substantially more unstable than other modes. The time required for them to emerge as dominant structures can therefore be much longer than their individual *e*-folding times. For climatological flows, this emergence time is too long for the scenario to be plausible. Second, the most unstable modes are often highly sensitive to small changes in the background flow and the linear model used in the eigenanalysis. If the properties of the most unstable eigenmodes are uncertain, then so must be any predictions of eddy statistics based on them.

Partly to circumvent these difficulties, Branstator (1995) hypothesized that the synoptic eddy statistics associated with any background flow may be approximated as the statistics of random initial disturbances evolving linearly over a short time interval τ_b on that background flow. Applying this idea to the prediction of the synoptic eddy statistics associated with a GCM's representative background flows, he was able to reproduce many features of those statistics. His success helps retain confidence in linear theories of eddy statistics, and also draws the focus away from the most unstable eigenmodes. It is interesting that Branstator found his results to be sensitive to the choice of τ_b, reporting that the best results were obtained for $\tau_b \sim 5$ days. Presumably, for $\tau_b \sim 0$, his predicted eddy variance field does not have time to evolve significantly away from the globally uniform initial distribution, and for $\tau_b > 10$ days, it asymptotes to the amplitude structure of the most unstable eigenmode, which in his case is a poor match to the GCM's synoptic eddy variance. To obtain the best match, therefore, an intermediate value has to be chosen so that many, if not all, of the eigenmodes contribute to the eddy statistics.

Branstator's results are encouraging, but his approach also has difficulties. Because the eddy variances at time $t = 0$ and $t = \tau_b$ are not the same, his theory of the eddy statistics is not statistically stationary: it matters what the time origin is. The theory is also silent about what happens after $t = \tau_b$, and why it is not important in determining the eddy statistics. Surely the higher amplitude eddies at these later times must also contribute to the eddy statistics, especially the momentum fluxes?

An entirely different approach to the problem of predicting extratropical synoptic eddy statistics has been advocated by Farrell and collaborators. In a series of papers (Farrell and Ioannou 1993, 1994, 1995; Delsole and Farrell 1995; Farrell 1989) they propose that the eddies are best viewed as stochastically forced disturbances evolving on a baroclinically *stable* background flow. Eddies can still grow on such a flow, for a finite time, through local energy extraction from the background shears. If the quadratic nonlinearities are approximated as stochastic excitation plus an augmented dissipation, as done in many early studies of homogeneous turbulence (e.g., Kraichnan 1959; Leith 1971), the governing equations reduce to a (multi-) linear Markov process. The extensive theory of stationary Markov processes can then be employed to deduce the statistics of the eddies in statistical equilibrium. The results of Farrell and Ioannou (1994) and Delsole and Farrell (1995) suggest that this approach can explain certain features of observed transient eddy energy and heat flux spectra that baroclinic instability theory cannot. But perhaps the most attractive feature of this alternative theory is that it is statistically stationary. The theory also takes into account, however crudely, two of the most important nonlinear aspects of synoptic eddy evolution: saturation and excitation. The latter conceivably represents what synopticians sometimes refer to as the seeding of new weather systems by the ''debris'' of old systems.

Farrell and collaborators have thus far discussed their ideas in zonally symmetric contexts. Our principal goal here is to investigate to what extent their alternative viewpoint is quantitatively useful in deducing the observed zonally varying synoptic eddy statistics associated with observed zonally varying background flows. To this end, we linearize a two-level hemispheric quasigeostrophic model about representative observed flows, stabilize it with an extra dissipation, force it with Gaussian white noise, and compare the stationary statistics of the resulting eddies with observations.

To focus the discussion and establish terminology, we begin with some theoretical preliminaries in section 2. Section 3 describes the observational datasets and data filtering procedures, the two-level model equations, and the procedure for obtaining the eddy statistics in statistical equilibrium using the theory of stationary Markov processes. Results for the climatological winter eddy statistics are presented in section 4. Results for the seasonal and interannual variations of the statistics are presented in section 5. Sensitivity to the specification of the extra damping is discussed in section 6. Section 6 also considers the sensitivity to whether the Gaussian

white forcing is specified as white in the streamfunction, rotational kinetic energy, or vorticity norms; that is, whether the streamfunction, kinetic energy, or vorticity on different spatial scales are excited equally by it. Section 7 follows with a discussion and conclusion.

2. Theoretical preliminaries

Consider the evolution equation for synoptic eddies in the form

$$\frac{d\tilde{\mathbf{x}}}{dt} = \mathbf{L}\tilde{\mathbf{x}} + \tilde{\mathbf{n}} + \tilde{\mathbf{F}}, \tag{1}$$

where $\tilde{\mathbf{x}}$ is a vector of eddy expansion coefficients in say a spherical harmonic basis, $\mathbf{L}$ is the dynamical operator of the model linearized about a specified background flow in that basis, $\tilde{\mathbf{n}}$ denotes nonlinear terms, and $\tilde{\mathbf{F}}$ represents forcing. We will assume that (1) has been written in such a way that $\tilde{\mathbf{x}}$ is a real vector and $\mathbf{L}$ is a real matrix. Note that $\mathbf{L}\tilde{\mathbf{x}}$ includes eddy dissipation terms in addition to the terms linearized about the specified background flow. Our aim in this paper is to relate the covariance matrices

$$\mathbf{C}_0 = \langle \tilde{\mathbf{x}}(t)\tilde{\mathbf{x}}^{\mathrm{T}}(t)\rangle, \tag{2a}$$

$$\mathbf{C}_\tau = \langle \tilde{\mathbf{x}}(t+\tau)\tilde{\mathbf{x}}^{\mathrm{T}}(t)\rangle, \tag{2b}$$

of the synoptic eddies, where angle brackets denote an ensemble average (which is often estimated as a time average) to the structure of the background flow. To this end, we will approximate the sum of the nonlinear and forcing terms in (1) as

$$\tilde{\mathbf{n}} + \tilde{\mathbf{F}} = \mathbf{D}\tilde{\mathbf{x}} + \tilde{\mathbf{F}}_s, \tag{3}$$

where $\tilde{\mathbf{F}}_s$ is Gaussian white noise and $\mathbf{D}$ is a damping operator. Equation (3) is only expected to hold on average, not for every realization. As discussed by DelSole and Farrell (1995), (3) may be thought of as a parameterization of quadratic nonlinearities in the spirit of classical studies of homogeneous turbulence (Kraichan 1959; Leith 1971). With this approximation, (1) becomes

$$\frac{d\tilde{\mathbf{x}}}{dt} = (\mathbf{L}+\mathbf{D})\tilde{\mathbf{x}} + \tilde{\mathbf{F}}_s = \mathbf{B}\tilde{\mathbf{x}} + \tilde{\mathbf{F}}_s. \tag{4}$$

We will specify $\mathbf{D}$ such that $\mathbf{B}$ is a stable operator—that is, all its eigenvalues have negative real parts. Equation (4) then becomes a multivariate linear Markov model of the synoptic eddies.

The general properties of a model such as (4) have been discussed recently in detail in other geophysical contexts by Penland and Ghil (1993), DelSole and Farrell (1995), Penland and Sardeshmukh (1995), and Newman et al. (1997, hereafter NSP). Its most important property is that without the forcing $\tilde{\mathbf{F}}_s$, all eddies eventually decay. In a multivariate system, however, that decay need not be monotonic. As noted by numerous authors, if the maximum singular value of the operator $\exp(\mathbf{B}\tau)$ is greater than 1 for some τ, then eddy growth is possible over the interval $[t, t+\tau]$. Nevertheless, to achieve a statistically stationary state, the general decaying tendency of the eddies must be balanced by forcing. This balance condition, known in the stochastic dynamical systems literature as a fluctuation–dissipation relation (FDR) (e.g., see Gardiner 1985) may be expressed as

$$\mathbf{B}\mathbf{C}_0 + \mathbf{C}_0\mathbf{B}^{\mathrm{T}} + \mathbf{Q} = 0, \tag{5}$$

where $\mathbf{Q} = \langle \tilde{\mathbf{F}}_s(t)\tilde{\mathbf{F}}_s^{\mathrm{T}}(t)\rangle\, dt$ is the covariance matrix of the stochastic white noise forcing. Equation (5) is sometimes also referred to as the ''Lyapunov equation'' in the literature (e.g., Farrell and Ioannou 1993). A rigorous derivation involves the Fokker–Planck equation (Arnold 1974) and can be found, for example, in Penland and Matrosova (1994). The only assumption made in going from (4) to (5) is that $\mathbf{B}$ is stable. It is important to note also that in order for (5) to be valid $\mathbf{Q}$ must be symmetric but not necessarily diagonal—that is, that $\tilde{\mathbf{F}}_s$ be white in time but not necessarily white in space. Equation (5) links the covariance structure of the eddies, $\mathbf{C}_0$, to the structure of the background flow, $\mathbf{B}$, and to the covariance structure of the forcing, $\mathbf{Q}$. Given $\mathbf{B}$ and $\mathbf{Q}$, therefore, one can solve for $\mathbf{C}_0$. Further, the lag-covariance matrices $\mathbf{C}_\tau$ in any dynamical system of the form (4) are related to $\mathbf{C}_0$ as

$$\mathbf{C}_{\tau>0} = \exp(\mathbf{B}\tau)\mathbf{C}_0 \tag{6}$$

(Penland 1989) and can therefore also be determined once $\mathbf{C}_0$ is known.

To simplify even further, we hypothesize that the geographical coherence of the forcing is unimportant in (4) and (5), and approximate $\mathbf{Q}$ as $\mathbf{Q} = \varepsilon\mathbf{I}$, where $\mathbf{I}$ is the identity matrix and ε is a scaling constant. Our parameterization of the eddy statistics then becomes

$$\mathbf{B}\mathbf{C}_0 + \mathbf{C}_0\mathbf{B}^{\mathrm{T}} + \varepsilon\mathbf{I} = 0, \tag{7a}$$

$$\mathbf{C}_{\tau>0} = \exp(\mathbf{B}\tau)\mathbf{C}_0, \tag{7b}$$

$$\mathbf{C}_{\tau<0} = \mathbf{C}_{\tau>0}^{\mathrm{T}}. \tag{7c}$$

Given any background flow, that is, $\mathbf{B}$, we determine $\mathbf{C}_0$ through (7a) and $\mathbf{C}_\tau$ through (7b) and (7c). Note that (7a) implies that *if the background flow changes, the eddy statistics change in such a way that the symmetric part of* $\mathbf{B}\mathbf{C}_0$ *remains the same as before.* This is the essence of our parameterization. Note also that our prediction of a *change* in $\mathbf{C}_0$ does not depend upon an explicit specification of $\mathbf{Q}$ in (5). We only need $\mathbf{Q}$ to predict the actual $\mathbf{C}_0$, and will show below that specifying $\mathbf{Q} = \varepsilon\mathbf{I}$ works quite well.

If $\tilde{\mathbf{x}}_\omega$ is the Fourier transform of the multivariate Markov process $\tilde{\mathbf{x}}(t)$ in (4), then its covariance matrix in the frequency domain is

$$\mathbf{C}_\omega = \langle \tilde{\mathbf{x}}_\omega \tilde{\mathbf{x}}_\omega^{\mathrm{T}*}\rangle = (\omega\mathbf{I} + i\mathbf{B})^{-1}\mathbf{Q}(\omega\mathbf{I} - i\mathbf{B}^{\mathrm{T}})^{-1}, \tag{8}$$

where the superscript T* denotes complex conjugate transpose. The power spectra of all components of $\tilde{\mathbf{x}}_\omega$,

as well as their cross-spectra, are given by (8). Now, since $\mathbf{C}_\omega$ and $\mathbf{C}_\tau$ form a Fourier transform pair,

$$\mathbf{C}_\tau = \frac{1}{2\pi}\int_{-\infty}^{+\infty} \mathbf{C}_\omega e^{-i\omega\tau}\, d\omega, \tag{9a}$$

$$\mathbf{C}_\omega = \int_{-\infty}^{+\infty} \mathbf{C}_\tau e^{-i\omega\tau}\, d\tau. \tag{9b}$$

Solving (7), for all τ, thus yields not only complete information on the spatial structure of the eddies but their Fourier spectra as well.

We emphasize again that nothing about the *mathematical* development presented here is new. Once the assumptions leading to (4) are made, Eqs. (5)–(9) follow from the well-developed theory of stationary linear Markov processes. However, ours is the first comprehensive evaluation of the ability of such a model to explain the observed zonally varying statistics of synoptic eddies.

One may ask why our model should be considered a model of synoptic eddy statistics and not the full spectrum of transient eddies. NSP examined whether the FDR for a barotropic model linearized about the observed 300-mb flow could account for the observed statistics of low-frequency anomalies in the atmosphere. They found that although the model could be tuned to produce fairly realistic zero-lag covariances, the simulated time lag-covariances did not match observations very well. They concluded that the details of forcing and nonlinear interactions with other frequency bands are important in the dynamics of low-frequency transients. We do not expect our model to do any better with low-frequency eddies. Rather, our aim is to see if a simple stochastic *baroclinic* model can simulate the statistics of higher-frequency synoptic eddies.

Some caveats are in order. The parameterization problem is meaningfully posed only for ensembles that include a sufficiently large number of synoptic eddy events that their statistics can be reliably defined. For ensemble averages defined as time averages, this suggests that one should consider averages over at least one, and preferably many, 90-day seasons. We will consider the problems of deducing the 13-winter (DJF) average eddy statistics for 1982–95 given the 13-winter average flow, the differences between the 13-yr average eddy statistics for northern midwinter (January) and midspring (April) given the difference between the 13-yr mean flows for these months, and finally the anomalous eddy statistics for individual winters, given the anomalous flows for those winters. From sampling considerations alone, one would expect some degradation in the answers to these problems as the sample size is reduced.

There is, however, another, and perhaps even more important, reason as to why one should expect a degradation in the answers for smaller sample sizes. Any parameterization problem is well posed only to the extent that there is a clear temporal and spatial scale separation between the eddies and the mean flow, that is, a clear spectral gap. We define our synoptic eddies as eddies with timescales shorter than 8 days, and our mean flow as flow with timescales longer than 90 days. It might therefore appear that we have adequate scale separation. It is, however, important to bear in mind that there is actually no spectral gap in the observations. The spectrum of the observed variability is predominantly red, and eddies with timescales between 10 and 90 days may also be expected to affect the synoptic eddy statistics. One could thus observe, in principle, different 90-day mean synoptic eddy statistics associated with the same 90-day mean flow. Since the intermediate timescale eddies are unaccounted for in our analysis, they contribute, to the extent that they affect the synoptic eddies, an unparameterized portion to the synoptic eddy statistics in our problem. One could reasonably expect this contribution to be smaller for larger ensembles (such as climate means), particularly if it is a linear function of the intermediate timescale eddies (i.e., if a positive 10–90-day anomaly has the same effect on the synoptic eddies as an identical negative anomaly). For individual winters, however, it could be relatively large, and remains to be determined.

Our linear model $\mathbf{L}$ in (1) will be a two-level, hemispheric, quasigeostrophic model linearized about representative observed zonally varying flows at 400 and 800 mb. We will specify $\mathbf{D}$ in (4) as a simple linear drag $\mathbf{D} = -\alpha\mathbf{I}$. The scaling constant ε in (7) will be chosen so that the global maximum of rotational eddy kinetic energy obtained via (7) matches observations. Maps of the eddy streamfunction variance, kinetic energy, vorticity, and heat fluxes predicted by (7) will then be compared with the corresponding observed quantities.

Finally, we stress again that even if $\mathbf{B} = \mathbf{L} + \mathbf{D}$ is a stable operator, this does not imply that all eddy growth is associated with the stochastic forcing. As mentioned above, if $\exp(\mathbf{B}\tau)$ has singular values greater than 1, as is true in our system, then deterministic (as opposed to stochastic) eddy growth is possible over the interval $[t, t + \tau]$. The energy for this growth comes from the background flow, not the forcing. Indeed we will make a case that nearly 75% of the domain-integrated eddy variance in the statistically equilibrated system (4) comes from the background flow, and only about 25% from the stochastic forcing. Locally, in the jet regions where the energy source associated with the background flow shears is strongest, the relative importance of the energy source associated with the stochastic forcing is even less.

3. Data, equations, and solution procedure

a. Observational data and processing

The data used in this study were derived from the reanalysis dataset (Kalnay et al. 1996) produced by the National Centers for Environmental Prediction (NCEP). We utilize global 400-mb, 700-mb, and 850-mb wind fields sampled four times daily over the period 1982–

95. Winds at 800 mb were estimated by linear interpolation in the natural logarithm of pressure between 700 and 850 mb. Spherical harmonic coefficients of the 400-mb and 800-mb angular velocity (winds multiplied by cosine of latitude) were then calculated from the 2.5° gridded data using the SPHEREPACK[1] package and truncated to T31 resolution. Only the nondivergent winds were used in the analysis; these were obtained from the spectral coefficients of the vorticity field. Finally, bandpass filtered data were obtained by applying a 1–8-day bandpass 251-point Lanczos filter (see Sardeshmukh et al. 1997) to the 400-mb and 800-mb streamfunction coefficient time series.

b. The two-level model

We use a quasigeostrophic two-level model based on the linear balance equation (Lorenz 1960; Frederiksen 1983; often referred to as the P-model). After nondimensionalizing using the radius of the earth (a) as a length scale and the inverse of the earth's rotation rate (Ω^{-1}) as a timescale, the governing equations may be written:

$$\frac{\partial \nabla^2 \psi_j}{\partial t} + J(\psi_j, \nabla^2 \psi_j + 2\mu) + \nabla \cdot (2\mu \nabla \chi_j) = -((2 - j) r_M + \nu \nabla^4) \nabla^2 \psi_j, \tag{10}$$

$$\frac{\partial}{\partial t}(\phi_2 - \phi_1) + \frac{1}{2} J(\psi_1 + \psi_2, \phi_2 - \phi_1) + \sigma \omega_{3/2} = -(r_T + \nu \nabla^4)(\phi_2 - \phi_1), \tag{11}$$

$$\nabla^2(\phi_2 - \phi_1) = \nabla \cdot [2\mu \nabla (\psi_2 - \psi_1)], \tag{12}$$

where

$$J(A, B) = \frac{\partial A}{\partial \mu}\frac{\partial B}{\partial \lambda} - \frac{\partial B}{\partial \mu}\frac{\partial A}{\partial \lambda},$$

ψ is streamfunction, ϕ is geopotential, χ is velocity potential, μ is the sine of latitude, $\omega = dp/dt$, and (r_M, r_T, ν) are damping parameters. The subscript $j = 1$ (2) denotes the 800-mb (400-mb) level, while the subscript 3/2 denotes the 600-mb level. The variables ψ, χ, ϕ, and ω are nondimensionalized by $(\Omega a)^2$, $(\Omega a)^2$, Ωa^2, and $\Omega \Delta p$, respectively, where $\Delta p = p_2 - p_1 = -400$ mb. The static stability parameter σ is assumed to be a constant, given by

$$\sigma = \frac{-\Delta\pi \Delta\Theta}{\Omega^2 a^2}, \tag{13}$$

where $\Delta\pi$ is the difference between the Exner function [$\equiv c_p(p/p_0)^{R/C_P}$] at 400 and 800 mb and $\Delta\Theta$ is the mean potential temperature difference between 400 and 800 mb. For all of the results presented here, the dimensional values of the lower-level Rayleigh damping (r_M), the thermal damping (r_T), and the coefficient of the biharmonic diffusion (ν) are fixed at 2/5 day^{-1}, 1/7 day^{-1}, and 2.338×10^{16} m^4 s^{-1}, respectively. The stability parameter is fixed by specifying $\Delta\Theta = 15$ K.

The horizontal boundary conditions are

$$\omega_{5/2} = 0 \quad \text{and} \quad \omega_{1/2} = J(\psi_1, h), \tag{14}$$

where h is topographic height (scaled by $\rho_0 g/\Delta p$, where ρ_0 is a reference value of density at 1000 mb) and the subscript 1/2 (5/2) denotes the 1000-mb (200-mb) level. The velocity potential χ is related to ω through the continuity equation:

$$\nabla^2 \chi_j = (2j - 3)\omega_{3/2} + (2 - j)\omega_{1/2}. \tag{15}$$

The vorticity equation (10) is the prognostic equation for the model. Since geopotential and streamfunction are coupled through the balance equation (12), elimination of the time derivatives in (10) and (11) using $\partial/\partial t$ of (12) yields a diagnostic "ω equation" for the divergent flow (not shown).

c. Calculation of eddy statistics

Since (10) is the prognostic equation of our model, we define our state vector $\tilde{\mathbf{x}}$ in (4) as the vector of 400-mb and 800-mb streamfunction spherical harmonic coefficients. The linearized version of the two-level model may be used to construct $\mathbf{L}$, the matrix representing the linearized dynamical operator acting on $\tilde{\mathbf{x}}$. Here we use the observed nondivergent seasonally averaged flow at 400 and 800 mb to determine the basic state, with the static stability σ and the damping coefficients (r_M, r_T, ν) fixed at the values given previously.

The operator $\mathbf{D}$ in (4) is chosen to be a linear damping on the state variables, $\mathbf{D} = -\alpha\mathbf{I}$, where $\mathbf{I}$ is the identity matrix and α is a positive real scalar constant. It may be incorporated into the model without changing the eigenvectors or the imaginary parts of the eigenvalues of $\mathbf{L}$ by simply shifting the real parts of the eigenvalues by α. Unless otherwise noted, α is set to 1/10 day^{-1}, which is more than sufficient to stabilize $\mathbf{B} = \mathbf{L} + \mathbf{D}$ for observed long-term seasonal mean basic states. Further discussion of the sensitivity of our results to α is given in section 6.

The only quantity remaining to be specified in (7) is ε, an arbitrary scaling constant that affects the overall amplitude of the solution, but not its structure. We set it so the predicted global maximum of rotational eddy kinetic energy matches observed maximum.

d. Solution procedure

The spherical harmonic expansion of the state variable is truncated at T31, yielding a 2048-element real state vector in (4). To further reduce the dimensionality, we

[1] FORTRAN source code available free from the National Center for Atmospheric Research (NCAR) via anonymous FTP (ftp.ucar.edu).

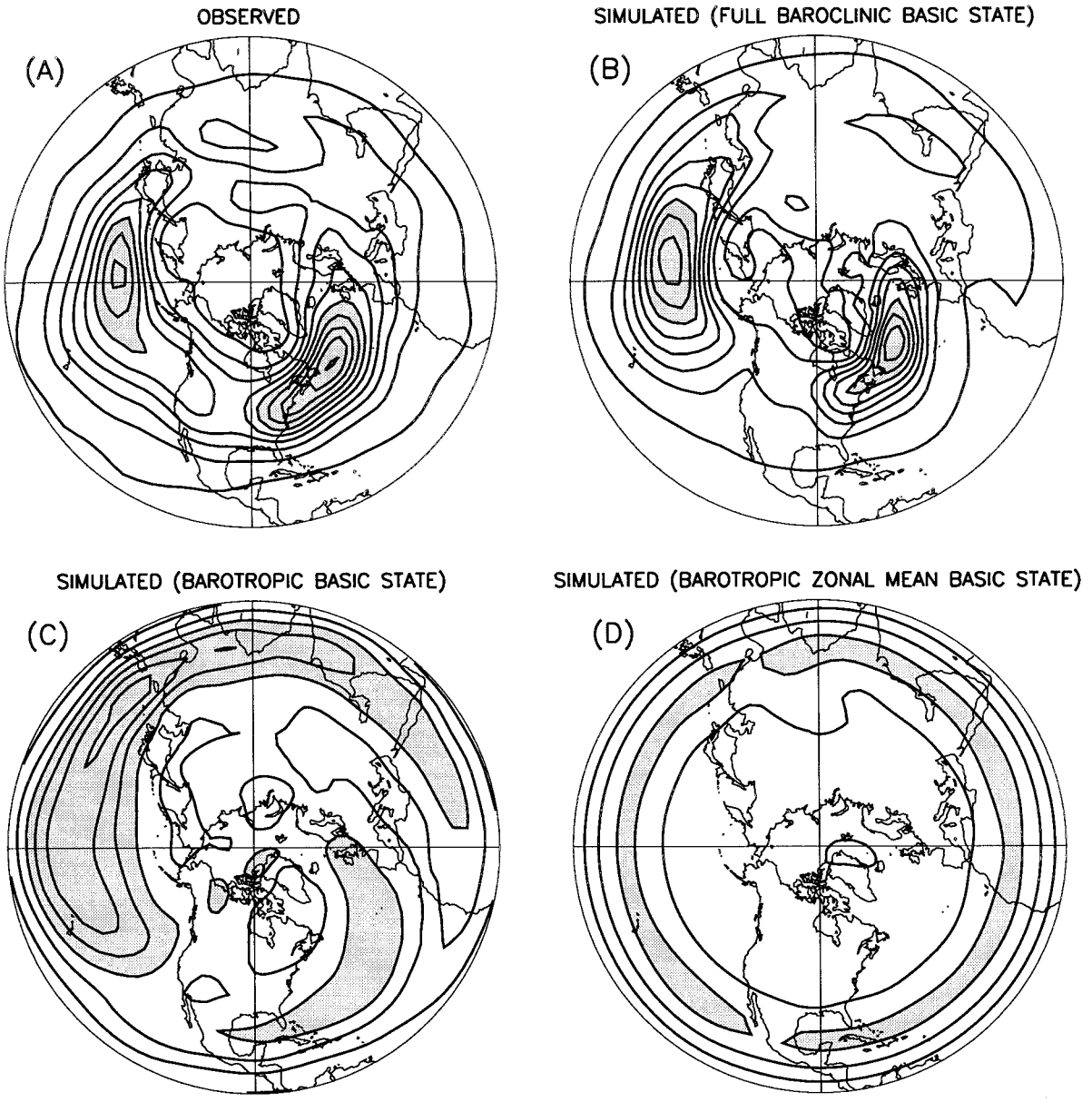

FIG. 1. Observed (a) and simulated (b), (c), and (d) DJF mean 400-mb 1–8-day bandpass streamfunction variance. In (b), the full DJF basic state is used. In (c), only the barotropic part of the DJF mean winds are included, while in (d) only the zonally symmetric part of the barotropic winds are included. Contour interval is 1×10^{13} m^4 s^{-2} in (a) and (b), 1.125×10^{12} m^4 s^{-2} in (c) and (d). Values greater than 6×10^{13} m^4 s^{-2} (6.75×10^{12} m^4 s^{-2}) are shaded in (a) and (b) [(c) and (d)]. In this and all following polar stereographic plots, the outermost latitude is 10°N.

reflect the Northern Hemisphere basic state onto the Southern Hemisphere, and also impose hemispheric symmetry on the eddies. This results in an $\mathbf{L}$ of rank 992. The FDR (7a) is then solved for $\mathbf{C}_0$ in the eigenspace of $\mathbf{B}$ [see appendix C in Penland and Sardeshmukh (1995)], and then transformed back to the spherical harmonic space. Then $\mathbf{C}_\tau$ is calculated from (7b) using the fact that $\exp(\mathbf{B}\tau) = \mathbf{E}\mathbf{\Lambda}\mathbf{E}^{-1}$, where $\mathbf{E}$ is the matrix with the eigenvectors of $\mathbf{B}$ as columns, λ_j are the eigenvalues of $\mathbf{B}$, and $\mathbf{\Lambda}$ is a diagonal matrix with elements $\exp(\lambda_j\tau)$. Finally, $\mathbf{C}_0$ and $\mathbf{C}_\tau$ are transformed from spectral to grid space, and their diagonal elements are displayed as variance and lag-covariance maps, respectively.

4. Results for the winter mean background flow

Using the 13-winter (DJF) mean winds to compute $\mathbf{L}$, we solve the FDR with the parameter settings given in section 3. Our state variable $\tilde{\mathbf{x}}$ contains the spherical harmonic coefficients for perturbation streamfunction, so $\mathbf{C}_0$ represents streamfunction covariance. The specification $\mathbf{Q} = \varepsilon\mathbf{I}$ therefore amounts to assuming that all the stream-

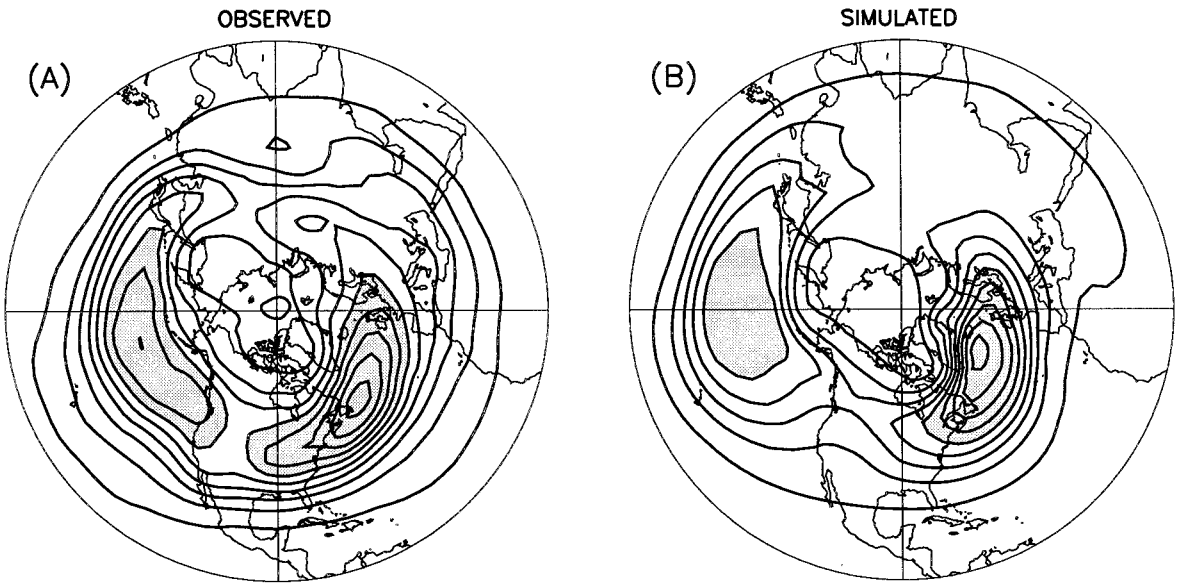

FIG. 2. Observed (a) and simulated (b) DJF mean 400-mb 1–8-day bandpass rotational kinetic energy. Contour interval is 15 $m^2\ s^{-2}$. Values greater than 90 $m^2\ s^{-2}$ are shaded.

function coefficients are excited equally, and independently, by our stochastic forcing $\tilde{\mathbf{F}}_s$. In general, the solution $\mathbf{C}_0$ of the FDR (7a) will depend upon the norm in which $\mathbf{Q}$ is specified to be white, that is, whether the streamfunction or, say, the vorticity coefficients are excited equally. Unless noted otherwise, all results in this paper are for $\mathbf{Q} = \varepsilon\mathbf{I}$ in the streamfunction norm. Sensitivity to the choice of norm is discussed further in section 6.

Figures 1a and 1b show the observed and predicted 400-mb DJF bandpass streamfunction variance, respectively. The scaling constant ε in (7a) has been chosen so that the maximum 400-mb rotational eddy kinetic energy of the solution matches observations (see Fig. 2). It is clear that the prediction is able to capture the most important features of the observed distribution, the Atlantic and Pacific storm tracks. The main deficiencies appear to be that the predicted Atlantic storm track is too far north and too little eddy activity penetrates the mean ridge in the eastern Pacific.

Figure 1c shows the result of a calculation in which

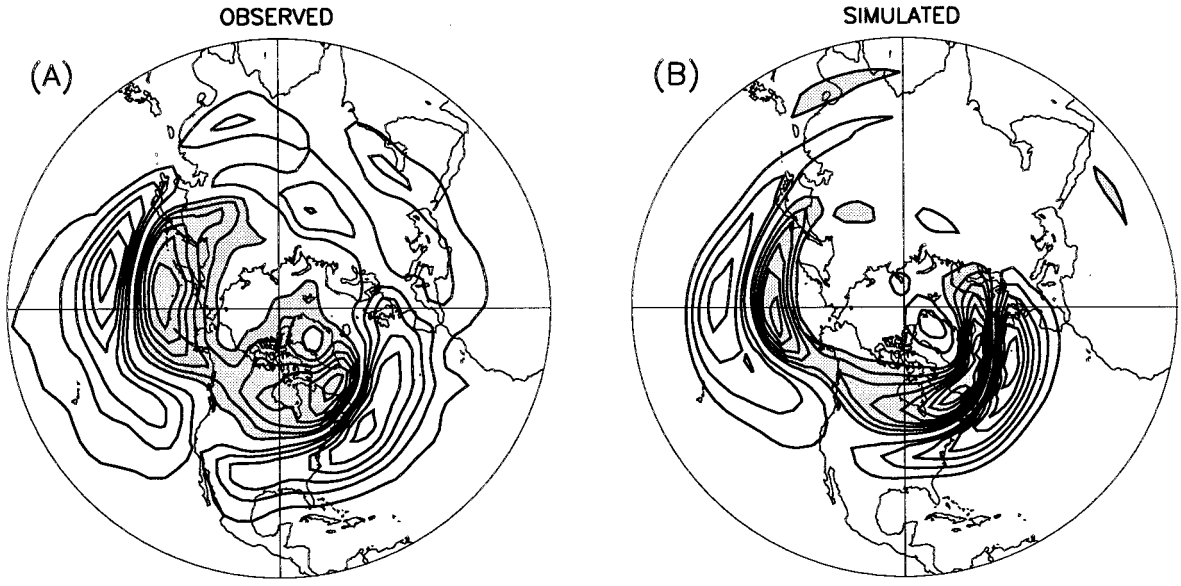

FIG. 3. Observed (a) and simulated (b) 400-mb streamfunction tendency associated bandpass eddy vorticity fluxes. See text for details of computational procedure. Contour interval is 3 $m^2\ s^{-2}$ in (a) and 6 $m^2\ s^{-2}$ in (b). Values less than $-3\ m^2\ s^{-2}$ are shaded in (a), $-6\ m^2\ s^{-2}$ in (b). The zero contour is omitted for clarity here and in Figs. 4–7.

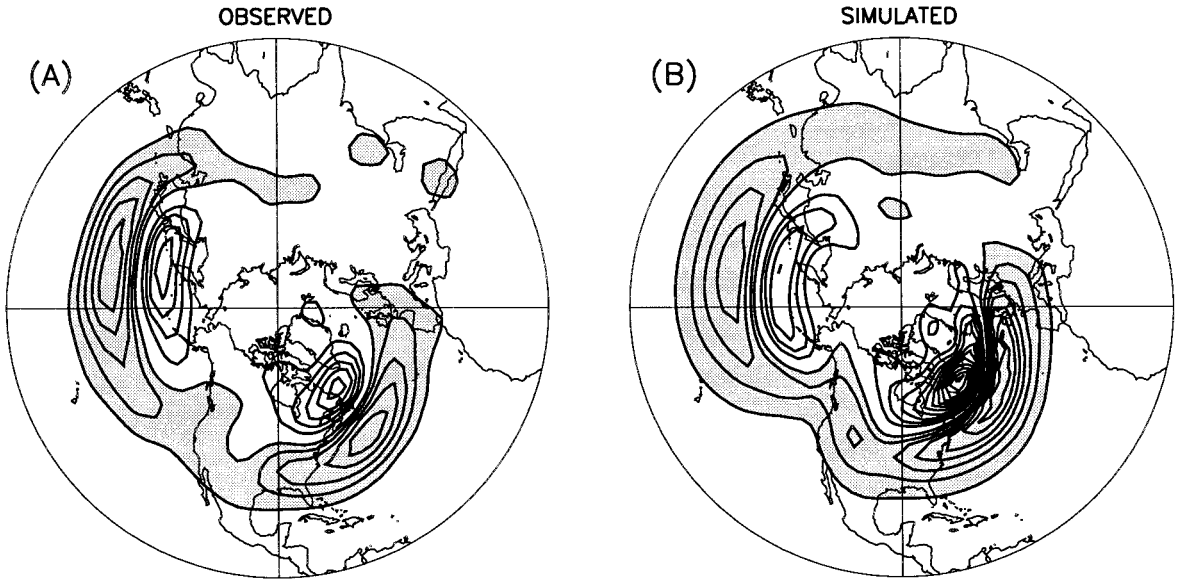

FIG. 4. Observed (a) and simulated (b) 400-mb streamfunction tendency associated with bandpass eddy heat fluxes. See text for details of computational procedure. Contour interval is 3 $m^2\ s^{-2}$; values less than $-3\ m^2\ s^{-2}$ are shaded.

only the barotropic part of the observed DJF winds are used to compute **L**. Since there are now no basic-state temperature gradients, Fig. 1c represents the eddy variance that is maintained solely by the stochastic forcing and barotropic energy conversions. The domain-integrated streamfunction variance is about 37% of that in Fig. 1b, indicating that baroclinic energy conversions play a dominant role in maintaining eddy variance in our stochastically forced, baroclinically stable model. To some extent, the barotropic calculation also yields localized regions of eddy variance over the Atlantic and Pacific oceans, although the dynamics of eddy growth supporting these "storm tracks" are clearly different from those in the full baroclinic calculation. When the zonally varying component of the barotropic basic flow is removed, the eddy variance is reduced even further (Fig. 1d), indicating that the barotropic energy source for the eddy variance in Fig. 1c is associated primarily with the zonally varying part of the barotropic deformation field. Finally, when only the solid body rotation component of the barotropic zonal

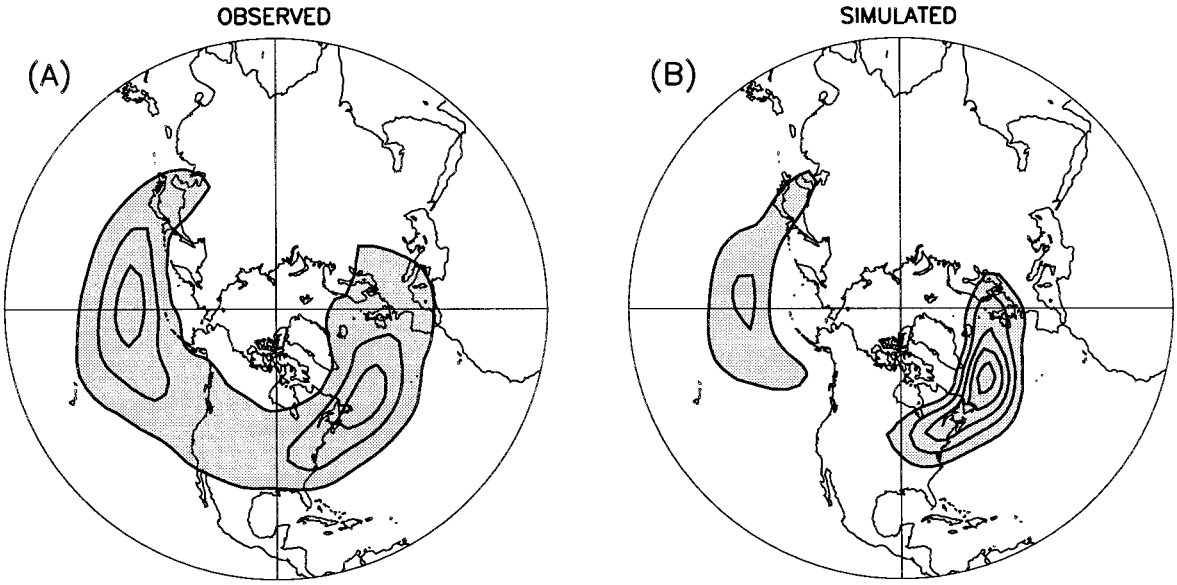

FIG. 5. Observed (a) and simulated (b) 1.5-day lag-covariance of DJF mean bandpass eddy streamfunction. Contour interval is 1×10^{13} $m^4\ s^{-2}$; values less than $-1 \times 10^{13}\ m^4\ s^{-2}$ are shaded.

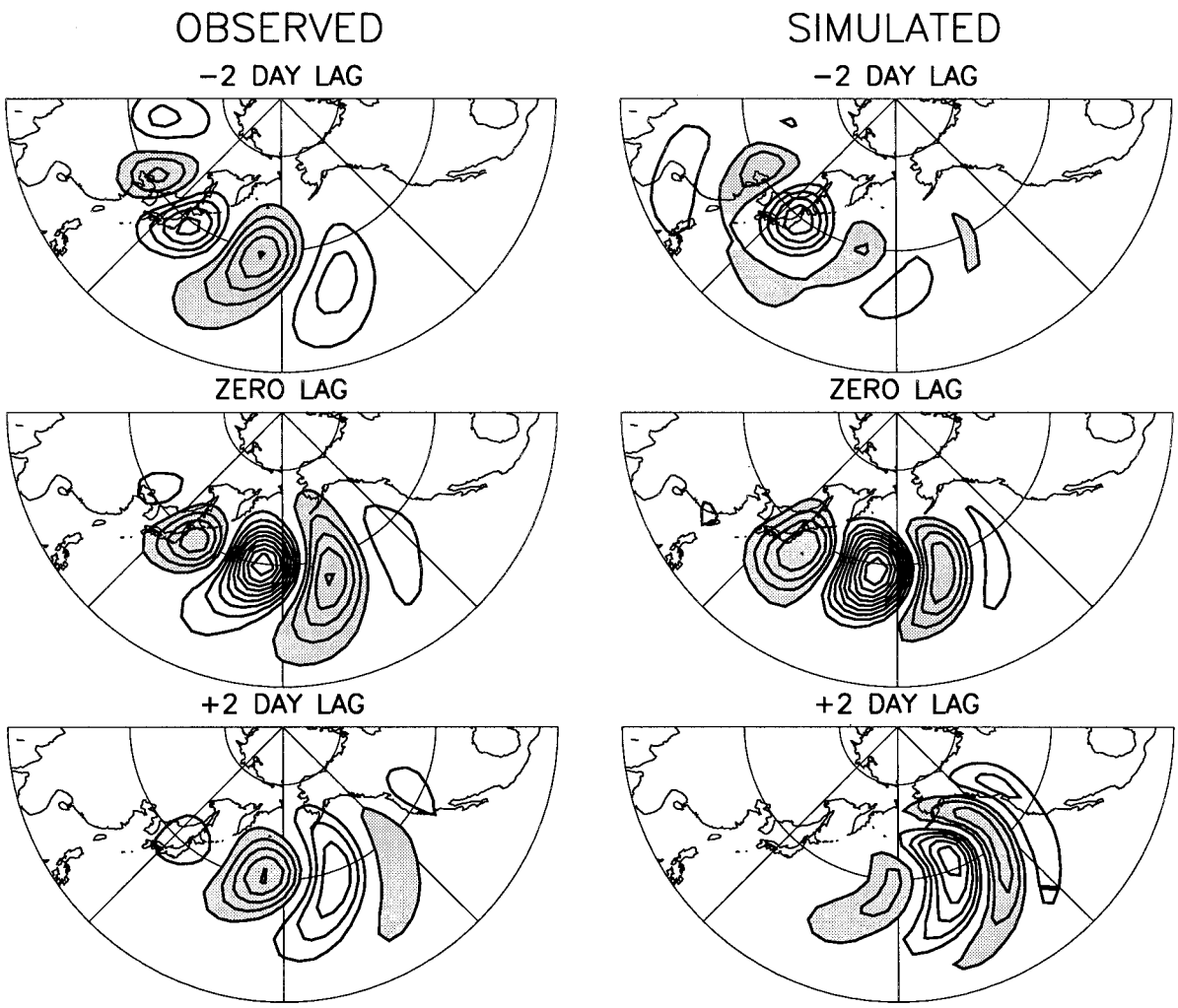

FIG. 6. Observed (left) and simulated (right) one-point lag-correlation maps for a base point at 38.966°N, 172.5°W. Contour interval is 0.1; values less than −0.1 are shaded.

wind is retained in the basic state, the domain integral of streamfunction variance (not shown) is reduced to about 27% of that in the full baroclinic case (Fig. 1b). For this extreme distortion of $\mathbf{L}$, there are no barotropic or baroclinic sources of energy for the eddies, and the variance is maintained solely by the stochastic forcing. We infer then that most of the eddy variance in the full baroclinic calculation (Fig. 1b) is associated with energetic interactions (mainly baroclinic) with the mean flow and is not forced *directly* by $\tilde{\mathbf{F}}_s$.

For any quantity $\tilde{\mathbf{y}} = \mathbf{M}\tilde{\mathbf{x}}$, the zero-lag covariance matrix of $\tilde{\mathbf{y}}$ is $\mathbf{M}\mathbf{C}_0\mathbf{M}^{\mathrm{T}}$, and its diagonal elements displayed in grid space constitute a variance map of $\tilde{\mathbf{y}}$. Figure 2 shows the observed and predicted rotational eddy kinetic energy at 400 mb determined in this manner. Again, the Atlantic and Pacific storm tracks, defined now in terms of rotational eddy kinetic energy instead of streamfunction variance, are quite well predicted. Note that both the predicted and observed Atlantic storm tracks are stronger than their Pacific counterparts, suggesting that at least some of the dynamics associated with the ''midwinter suppression'' of eddy activity in the Pacific noted by Nakamura (1992) are being captured by the model. We will return to this point in section 5a.

In addition to producing realistic variance maps, our theory (7) can also reproduce the observed heat and momentum fluxes, lag covariances, and one-point lag correlation maps quite well, as we will now demonstrate.

a. Simulated eddy fluxes of heat and momentum

Transports of heat and momentum by subweekly timescale eddies play an important role in maintaining the observed time-mean flow (Hoskins et al. 1983; Lau and Holopainen 1984; Hoskins and Sardeshmukh 1987a; Valdes and Hoskins 1989) as well as large-scale, persistent flow anomalies (e.g., Green 1977; Kok and Opsteegh 1985; Hoskins and Sardeshmukh 1987b; Held

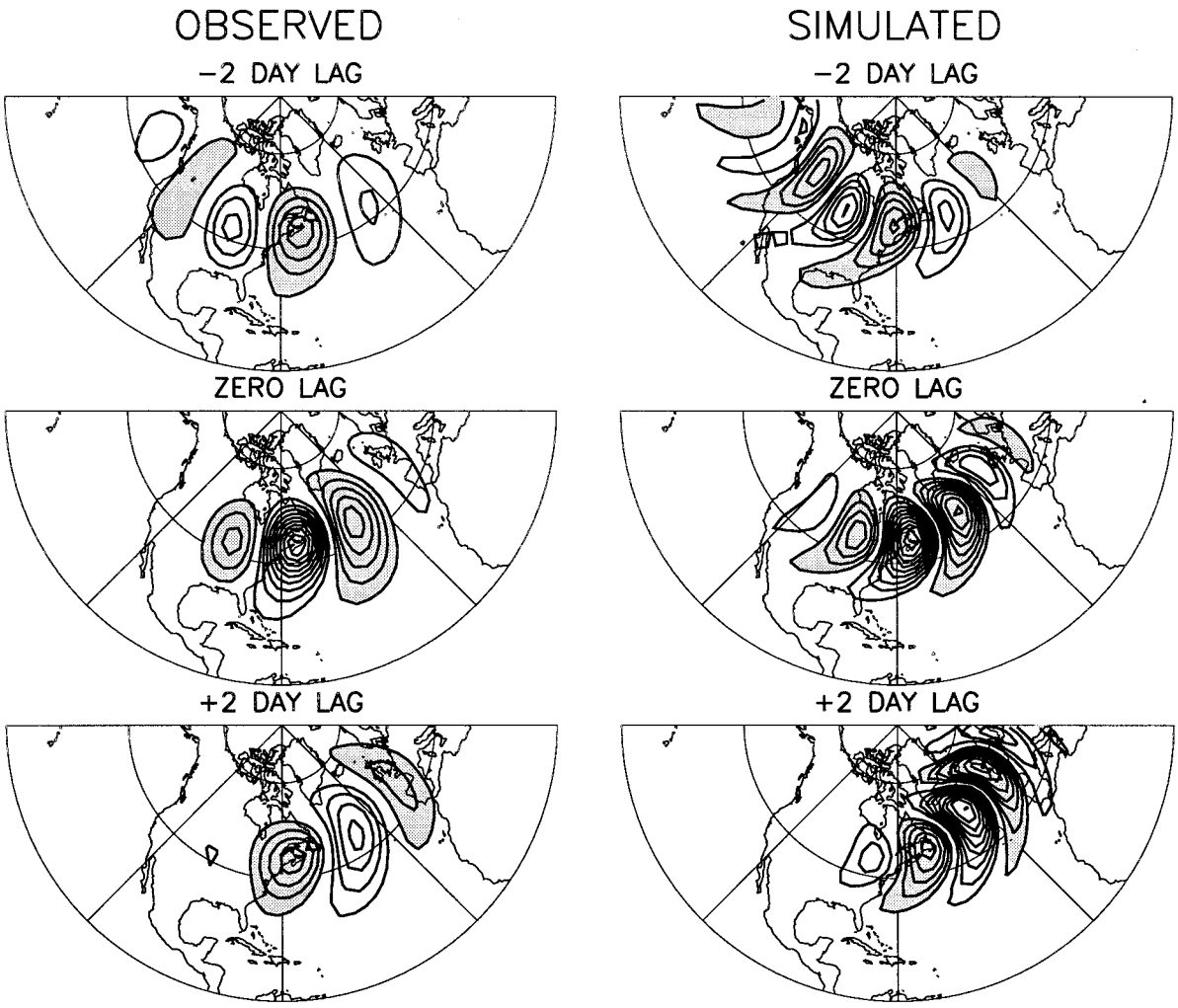

FIG. 7. Observed (left) and simulated (right) one-point lag-correlation maps for a base point at 46.3886°N, 63.75°E. Contour interval is 0.1.

et al. 1989; Nakamura and Wallace 1990). Although nonlinear feedbacks make it difficult to establish causal relationships, it would still be useful to know what changes in the storm tracks (including the attendant fluxes of heat and momentum) could be expected to accompany a change in the quasi-stationary large-scale flow. Such a ''storm-track model'' [e.g., our Eq. (7)] could then be used to parameterize the effects of synoptic eddies in a model of low-frequency atmospheric variability. For any such low-frequency model to be useful, however, one must first demonstrate that the storm track model accurately simulates the feedback of the synoptic eddies on the time-mean flow.

Our two-level model's time-mean vorticity equation may be written

$$\frac{\partial \nabla^2 \overline{\psi}_j}{\partial t} + J(\overline{\psi}_j, \nabla^2 \overline{\psi}_j + 2\mu) + \nabla \cdot (2\mu \overline{\nabla \chi}_j^{\text{mean}}) = -((2 - j)r_M + \nu\nabla^4)\nabla^2 \overline{\psi}_j - J(\overline{\psi_j'}, \overline{\nabla^2 \psi_j'}) - \nabla \cdot (2\mu \overline{\nabla \chi}_j^{\text{eddy}}), \quad (16)$$

where overbars represent a long time mean and primes indicate eddies. The quantities $\overline{\chi}_j^{\text{eddy}}$ and $\overline{\chi}_j^{\text{mean}}$ are obtained by solving the QG ''ω equation'' forced by transient eddy fluxes and mean advections, respectively. The mean streamfunction tendency associated with the synoptic eddy vorticity fluxes contains a part associated with the second term on the right-hand side of (16), as well as a contribution associated with the differences between the synoptic eddy vorticity fluxes at 400 and 800 mb, which enters through $\overline{\chi}_j^{\text{eddy}}$. These two components can be thought of as the barotropic and baroclinic components of the vorticity flux forcing, respectively. The contribution to the mean streamfunction tendency associated with transient eddy heat fluxes only enters through $\overline{\chi}_j^{\text{eddy}}$.

Figure 3 shows the streamfunction tendency associated with the synoptic eddy vorticity fluxes, obtained in this manner, from both observations and from the solution of our storm track model, the FDR (7a). The model captures the general tendency of the eddy mo-

mentum fluxes to accelerate the Pacific and Atlantic jets, although the values are about twice as large as observed.

The streamfunction tendency given by the predicted heat fluxes matches observations very well, in both geographical distribution and magnitude (Fig. 4). The only deficiency is the tendency for the simulated heat fluxes to be too strong in the Atlantic storm track. Our model appears not to have the problem noted by both Branstator (1995) and Frederiksen (1983); that is, when the eddy amplitudes are scaled so that the simulated momentum fluxes match observations, the heat fluxes are too large. In fact, our simulations appear to have the opposite problem; that is, the momentum fluxes over the Pacific are too large when the heat fluxes match observations. At this time we do not have an explanation for this behavior, but as pointed out by a reviewer, it may be related to the extreme vertical truncation of the model. Since the horizontal structure of the eddies is much better resolved than their vertical structure, baroclinic processes may be relatively less active than barotropic processes in our model. This can only be verified by increasing the vertical resolution of the model.

b. Lag-covariances and propagation characteristics

NSP examined whether the FDR for a barotropic model linearized about the observed 300-mb flow could account for the observed statistics of low-frequency flow anomalies in the atmosphere. They found that although the model could be tuned to produce fairly realistic zero-lag covariances, the corresponding lag-covariances did not match observations very well. Having established that our model (7a) produces realistic simulations of observed synoptic eddy variances and fluxes, we now examine to what extent it can also simulate the time lag-covariances. This is a more demanding test since we are now asking the model to simulate the characteristic timescales of the observed synoptic eddies, even though there are no preferred timescales in the forcing $\tilde{\mathbf{F}}_s$.

Figure 5 shows the 1.5-day lag streamfunction covariances computed from observed bandpass transients and the FDR (7). Both are predominately negative, with patterns similar to the zero-lag covariances (Figs. 1a and 1b) but with less amplitude. The predicted lag-covariance is somewhat weaker (stronger) than observed in the Pacific (Atlantic) storm track. Note that since the observations are subjected to a 1–8-day bandpass filter, the observed 5-day lag-covariance is small (see Fig. 10). The model's 5-day lag-covariance (not shown) is slightly larger than observed, indicating that some low-frequency motions are being excited by the white noise forcing. The contribution of these low-frequency motions to the eddy statistics shown here is, however, negligible.

One-point lead and lag-correlation maps are often used to illustrate the statistical structure and evolution of synoptic eddies (e.g., see Wallace et al. 1988). They represent a particular row (column) of $\mathbf{C}_\tau$ for negative (positive) τ, transformed to grid space and normalized by the corresponding diagonal element of $\mathbf{C}_0$. Figure 6 shows such maps for both observed and simulated 400-mb streamfunction at lags -2, 0, and $+2$ days for a base point near the western entrance of the Pacific storm track. There is a good correspondence between the observed and simulated maps, indicating that the structure and propagation characteristics of the synoptic eddies are well simulated in the Pacific storm track. The downstream energy propagation of eddy energy in the Pacific jet is slightly faster than observed, which may account for the fact that the simulated lag covariances are too weak (Fig. 5). Also, the horizontal tilts of the simulated eddies in the Pacific jet are too strong, consistent with the unrealistically large simulated momentum fluxes noted in the previous section.

The lag-correlation maps for a base point at the western entrance of the Atlantic storm track are shown in Fig. 7. Here discrepancies between simulated and observed eddies are more apparent, particularly for the $+2$ day correlations. The zonal scale of the simulated eddies is somewhat too short, the $+2$ day correlation is too large, and the eddies tend to propagate too far north and east, compared to the observed eddies.

One may ask why our model is able to succeed where NSP failed in simulating lag-covariance statistics, especially when, unlike NSP, no knowledge of the observed eddy statistics is used to specify $\mathbf{Q}$. The answer must be related to fundamental differences between the dynamics of high- and low-frequency atmospheric transients. It appears that the details of forcing and nonlinear interactions with other frequency bands are important in the dynamics of low-frequency transients, while energetic interaction with the background flow is the dominant process controlling the dynamics of high-frequency transients. In other words, the relative importance of the processes incorporated in $\mathbf{B}$ versus $\mathbf{Q}$ is opposite for the two types of variability.

c. Eddy growth: Deterministic or stochastic?

Since there is no exponential instability in our model (4), the simulated synoptic eddies must either be forced directly by the stochastic forcing or grow through transient energetic interactions with the background flow. Some indication of the relative roles of these processes was given in Fig. 1 and the accompanying discussion. Here we examine this issue in greater detail.

That the simulated eddy variance is much larger when the background flow has vertical and horizontal shears, and is geographically localized even though the forcing variance is spatially uniform, suggests that eddy interactions with the background flow are important. The maximum amplification (MA) curve (Penland and Sardeshmukh 1995; Borges and Sardeshmukh 1995; Sardeshmukh et al. 1997) summarizes the maximum growth of eddy variance that is possible in a linear system over

a time interval τ through such interactions. It consists of the square of the maximum singular values of the propagator $\mathbf{G}(\tau) = \exp(\mathbf{B}\tau)$ plotted as a function of τ. The initial eddy structures associated with this optimal growth are the corresponding right singular vectors of $\mathbf{G}$. The MA curve for our system, using the rotational kinetic energy norm (see section 6a), and derived from a $\mathbf{B}$ based on the 13-winter mean flow, is shown as the thick curve in Fig. 8. It shows that even though the background flow is asymptotically stable, amplification of global eddy rotational kinetic energy by as much as a factor of 12 is possible over 3 days through energetic interactions with the background flow. The thin curves in Fig. 8 show the evolution of perturbations optimized to give maximum growth over some selected time intervals. Note that perturbations optimized for short time intervals are highly suboptimal for longer time intervals, and eventually all perturbations decay.

The MA curve merely reveals the *possibility* of growth in a stable linear system in the absence of forcing. As discussed in Sardeshmukh et al. (1997), whether such growth actually occurs depends upon whether the state vector projects significantly on the subspace of the growing singular vectors. The fact that the variance maxima over the Pacific and Atlantic Oceans in Fig. 1b are more than one order of magnitude larger than in the calculation with no shears in the background flow (not shown) suggests that this does indeed happen in our system.

It is important to distinguish between eddy growth arising from interactions with the background flow and that arising from the stochastic forcing. The former is associated with the $\mathbf{B}\tilde{\mathbf{x}}$ term in (4) and is potentially predictable; the latter is associated with the $\tilde{\mathbf{F}}_s$ term and is unpredictable. If interactions with the mean flow are important, then (4) must also have some skill as a forecast model of synoptic eddies. According to (4), given an initial condition $\tilde{\mathbf{x}}$ (t), the most probable eddy state vector at time $t + \tau$ is $\tilde{\mathbf{x}}(t + \tau) = \mathbf{G}(\tau)\tilde{\mathbf{x}}(t)$ (Penland 1989). This is the same as making a forecast using (4) with the stochastic forcing ignored. Such forecasts were made from each one of the 4680 bandpass-filtered initial states in our 13 winter dataset, and verified against the observed bandpass-filtered $\tilde{\mathbf{x}}(t + \tau)$.

Figure 9 shows the local anomaly correlation of the observations and the $\tau = 36$ h forecasts of 400-mb streamfunction, defined as

$$r(\lambda, \phi, \tau) = \frac{\langle \psi(\lambda, \phi, t + \tau)\hat{\psi}(\lambda, \phi, t + \tau)\rangle}{\{\langle \psi(\lambda, \phi, t + \tau)\psi(\lambda, \phi, t + \tau)\rangle\langle \hat{\psi}(\lambda, \phi, t + \tau)\hat{\psi}(\lambda, \phi, t + \tau)\rangle\}^{1/2}}, \tag{17}$$

where the caret indicates a forecast value, and the angle brackets denote an ensemble average over the 4680 cases. The contour interval is 0.1, values greater than $+0.3$ are shaded, and zero skill is indicated by the thick contour. The model has positive forecast skill almost everywhere on the hemisphere, except in a small area around the pole. As expected from the discussion in the previous paragraph, it has the greatest skill (r exceeding 0.4) in the vicinity of the Pacific and Atlantic jets, where the $\mathbf{B}\tilde{\mathbf{x}}$ term in (4) is most important. Figure 9 may be contrasted with a similar figure for 36-h persistence forecasts, obtained by dividing the values in Fig. 5a with those in Fig. 1A. That figure is not shown here for brevity; it is has negative values between -0.3 and -0.5 everywhere, and is relatively featureless.

Figure 10 shows, as a function of the forecast lead time τ, the global pattern anomaly correlation

$$r_g = \frac{\langle \tilde{\mathbf{x}}(t + \tau)^{\mathrm{T}}\hat{\tilde{\mathbf{x}}}(t + \tau)\rangle}{\{\langle \tilde{\mathbf{x}}(t + \tau)^{\mathrm{T}}\tilde{\mathbf{x}}(t + \tau)\rangle\langle \hat{\tilde{\mathbf{x}}}(t + \tau)^{\mathrm{T}}\hat{\tilde{\mathbf{x}}}(t + \tau)\rangle\}^{1/2}} = \frac{\mathrm{Tr}(\mathbf{C}_\tau\mathbf{G}^{\mathrm{T}})}{\{\mathrm{Tr}(\mathbf{G}\mathbf{C}_0\mathbf{G}^{\mathrm{T}})\mathrm{Tr}(\mathbf{C}_0)\}^{1/2}} \tag{18}$$

of the observations and τ-day forecasts of the 400-mb and 800-mb bandpass-filtered streamfunction. Here $\mathbf{C}_\tau$ and $\mathbf{C}_0$ are the time-lag and zero-lag covariance matrices, respectively, of the *observed* bandpass eddies. The anomaly correlation drops below 0.2 after about day 2, but the predicted patterns remain positively correlated with the observed patterns out to at least 5 days. For comparison, the pattern anomaly correlation of the τ-day persistence forecasts, $r_{\mathrm{per}} = \mathrm{Tr}(\mathbf{C}_\tau)/\mathrm{Tr}(\mathbf{C}_0)$, is shown in Fig. 10 as the solid curve with filled squares. The QG model clearly outperforms persistence at all forecast ranges.

In summary, consistent with the enhancement of eddy variance in Fig. 1 near the jets associated with energetic eddy interactions with the mean flow, the model (4) does indeed have some forecast skill in those areas. A substantial portion of the eddy growth in those areas is deterministic, not stochastic. These statements can be made independent of the most uncertain parameter in our model, the extra damping parameter α, since the QG model anomaly correlations shown in Figs. 9 and 10 are independent of α.

5. Annual and interannual variations of the storm tracks

As discussed earlier, if our storm track model is to be useful as a parameterization of synoptic eddy statistics in a model of low-frequency variability, it should

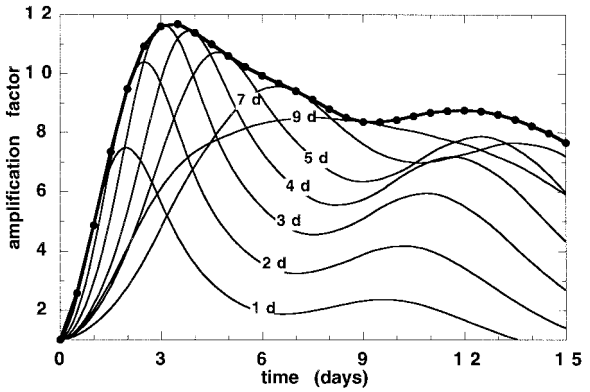

FIG. 8. Maximum amplification (MA) curve for DJF basic state, together with the evolution of selected optimal perturbations. Curves are labeled with optimization time in days. Amplification factor refers to increase in total rotational kinetic energy. Extra damping included in the **D** operator is 1/10 day^{-1}.

be able to predict the changes in those statistics associated with observed low-frequency changes of the background flow. We have tested our model in this regard by examining the sensitivity of the simulated storm tracks to the observed annual cycle and interannual variability of the background flow.

a. Annual cycle of storm tracks

Nakamura (1992) examined the annual evolution of the Northern Hemisphere storm tracks during the 6-month cold season (October through April). He found that although the Pacific jet is strongest in January, the Pacific storm track is actually weaker in January than in both November and April. The Pacific storm track in January is also weaker than the Atlantic storm track, even though the Pacific jet is stronger than the Atlantic jet. To see if our model can reproduce these aspects of the annual cycle, we have solved the FDR using long-term January and April mean states. As before, the parameter ε is set so that the simulated maximum eddy rotational kinetic energy at 400 mb matches observations, but *separately* in each case.

Figure 11 shows the observed and simulated 400-mb rotational eddy kinetic energy for the two cases. Consistent with observations, the simulated Pacific storm track is weaker than the Atlantic storm track in January, and stronger than the Atlantic storm track in April. However, if equal forcing amplitudes (i.e., the same ε) are used in the two cases, the model does not produce a weaker Pacific storm track in January than in April. Thus the model does not capture the midwinter minimum in the Pacific storm track. It is, however, able to simulate the relative amplitudes of the Pacific and Atlantic storm tracks in both winter and spring seasons. The model also captures the observed tendency of the downstream end of the Atlantic storm track to be more connected with the upstream end of the Pacific storm track in April than in January, associated with the enhanced propagation in April of the eddy activity over Northern Europe and Asia.

b. Interannual variability of the winter storm tracks

Extratropical seasonal mean circulation anomalies are known to be associated with significant storm track shifts (Lau 1988). The associated anomalous eddy momentum and heat fluxes have an important feedback on the anomalous seasonal flow (Kok and Opsteegh 1985; Held et al. 1989; Hoerling and Ting 1994). In this section we examine to what extent our stochastic model can reproduce the storm track shifts accompanying the seasonal mean circulation anomalies observed in the 13 northern winters of DJF 1982/83–1994/95.

We have solved the FDR (7a) for each of these 13 winters, but with a different α for each case, chosen such that the growth rate of the most unstable eigenmode of each winter basic state is $-1/20$ day^{-1}. The reason for this choice of damping is discussed in detail in section 6b. Briefly, without α, the growth rate for the most unstable eigenmode ranges from 0.0394 day^{-1} (for DJF 85/86) to 0.0966 day^{-1} (for DJF 93/94). It was found that the simulated eddy variance, Tr$\mathbf{C}_0$, is sensitive to α only when α is close to the *e*-folding time of the most unstable mode (see Fig. 16). Therefore, using a fixed α of 1/10 day^{-1} for all 13 cases resulted in very large amplitude storm tracks for DJF 1993/94. We chose a mean-flow-dependent α to avoid this nearly resonant behavior. We could have circumvented this by repeating all the calculations with a stronger α, say $\alpha = 1/7$ day^{-1}.

As discussed in section 2, both limited sampling and the neglect of intermediate (8–90 day) timescale eddies would prevent our model from accurately simulating the storm track anomalies for individual seasons. Even so, one would expect the model to simulate at least some of the statistics of the interannual variability of the storm tracks. Figure 12 shows the observed and simulated standard deviation of the 13 bandpass variance maps of 400-mb streamfunction obtained for the 13 winters. The model correctly captures the large interannual variability of the storm tracks in the eastern Pacific and Atlantic basins, albeit with considerably stronger amplitude than observed in the Pacific basin. Thus the model has some skill in simulating the observed interannual variability of the storm tracks, given the observed interannual variability of the winter mean flow.

The results of the 13 individual calculations are summarized in Table 1. For each winter, the table shows the hemispheric pattern correlation of the observed and simulated 400-mb anomalous streamfunction variance maps. The anomalous maps of the observed and simulated variances were obtained as departures from their respective 13-winter means, and smoothed to T12 resolution before calculating their pattern correlation. (We

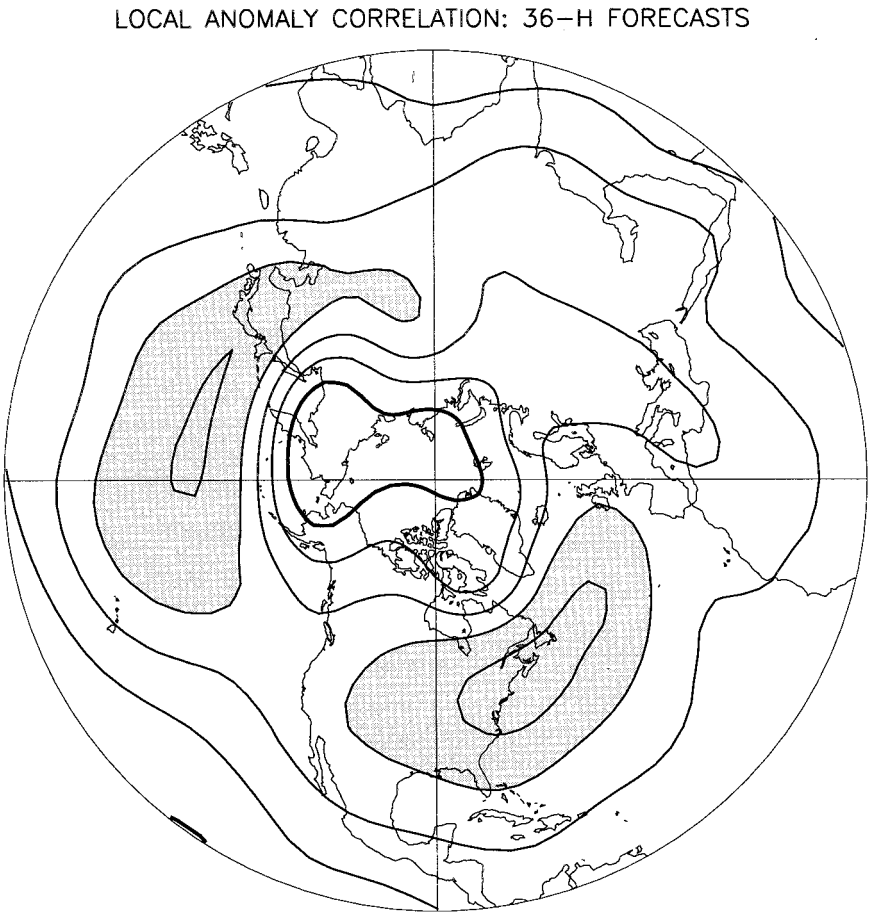

FIG. 9. Local anomaly correlation between observed bandpass-filtered 400-mb streamfunction and 36-h forecasts produced by the QG model. Contour interval is 0.1 with values greater than 0.3 shaded. See text for details.

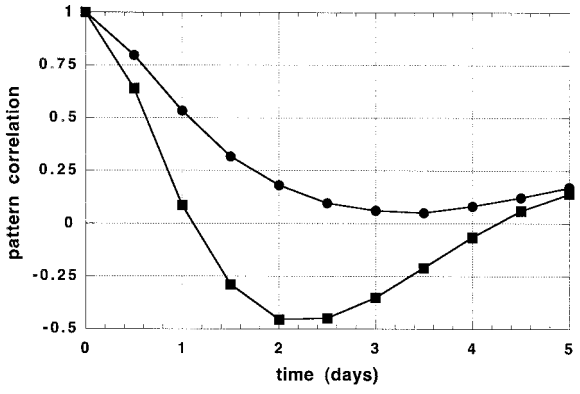

FIG. 10. The curve with solid circles shows pattern correlation as a function of forecast time for unforced linear integrations using (4) starting from observed bandpass streamfunction at 400 and 800 mb. The curve with solid squares shows pattern correlation for persistence forecasts. See text for details.

note in passing that the average of the 13 simulated variance maps is nearly identical to the variance computed using the 13-winter mean basic state shown in Fig. 1b.) The pattern anomaly correlation averaged over the 13 cases in Table 1 is only 0.3. This suggests that either 1) there are significant errors in our storm track model and/or 2) a large fraction of the anomalous synoptic eddy variance for an individual winter is not directly linked to that winter's anomalous mean flow. At present we do not have a way of deciding between these two interpretations.

Figure 13 shows the observed and simulated anomalous storm tracks for three winters: one with the best anomaly correlation (top), one with the worst (middle), and an ENSO case (bottom). In the best case (DJF 1994/95), the model appears able to capture virtually every detail of the observed storm track anomalies. On the other hand, it has virtually no skill in the worst case (DJF 1984/85). In the warm ENSO case of DJF 1982/83, the dominant features of the observed anomalous storm tracks are a southward shift and eastward extension of the Pacific storm track and a northward shift of

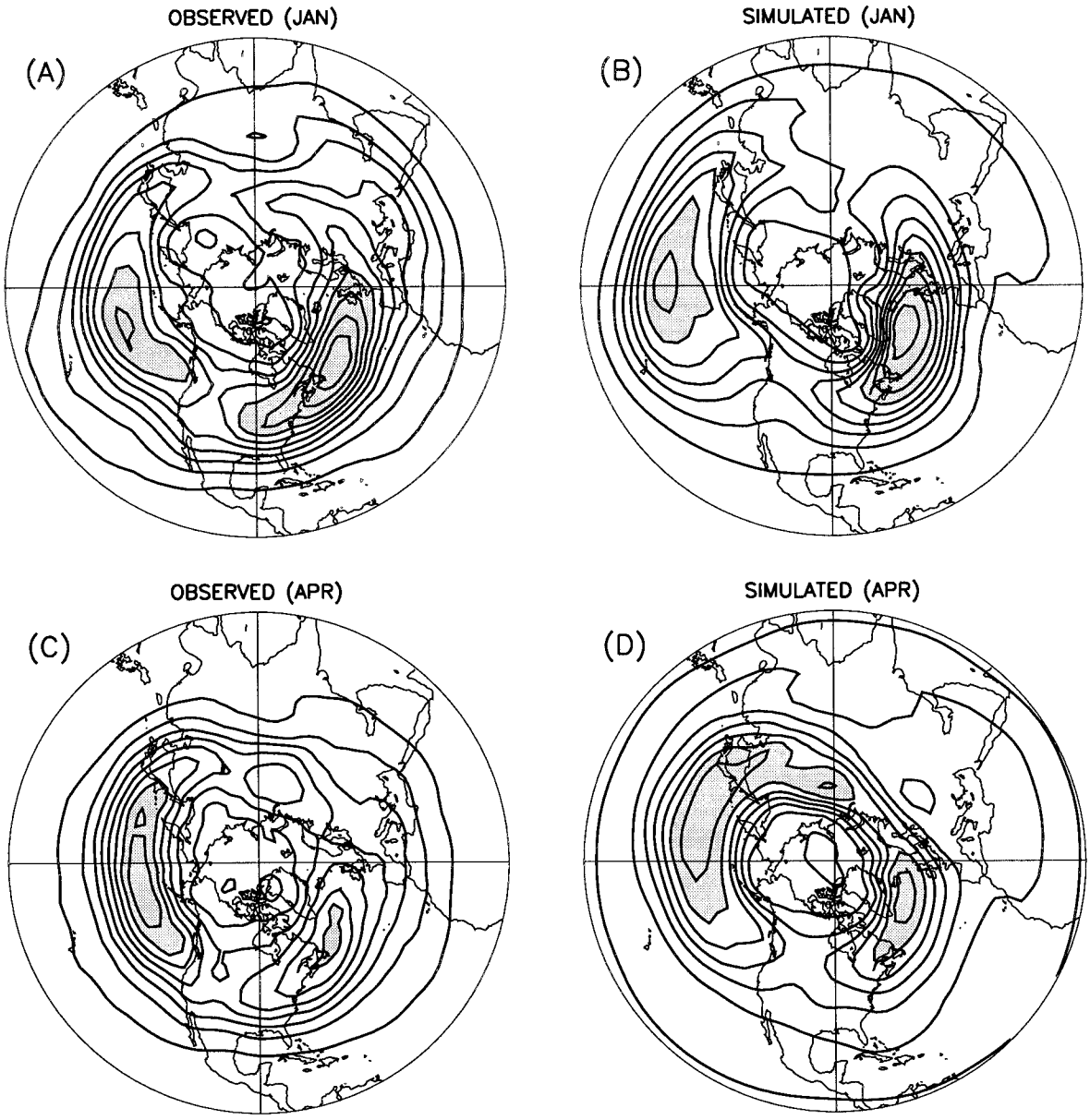

FIG. 11. Observed (left) and simulated (right) monthly mean 400-mb bandpass rotational kinetic energy for January (top) and April (bottom). Contour interval is 15 $m^2\ s^{-2}$; values greater than 105 $m^2\ s^{-2}$ are shaded.

the Atlantic storm track. These shifts are consistent with the observed anomalous southward and eastward extension of the Pacific jet, and the northward shift of the Atlantic jet, respectively. The latter is consistent with the particular phase of the North Atlantic oscillation (NAO) that was persistent during that winter. The stochastic model is able to capture the observed northward shift of the Atlantic storm track quite well. In the Pacific basin, the model does produce an eastward shift of the Pacific storm track as observed, but the negative anomalous streamfunction variance in the Gulf of Alaska is weaker than observed.

6. Sensitivity

a. Sensitivity to the choice of norm

Given that our state vector $\mathbf{x}$ in (4) is a vector of 400-mb and 800-mb streamfunction spherical harmonic coefficients Ψ_j, the specification $\mathbf{Q} = \varepsilon\mathbf{I}$ in (7a) amounts to assuming that all those coefficients are excited equally and independently by the stochastic forcing. In other words, $\mathbf{Q}$ is assumed to be white in the streamfunction norm. One may ask if our results depend strongly upon this assumption. To explore this, we have solved the FDR for the 13-winter mean DJF basic state assuming

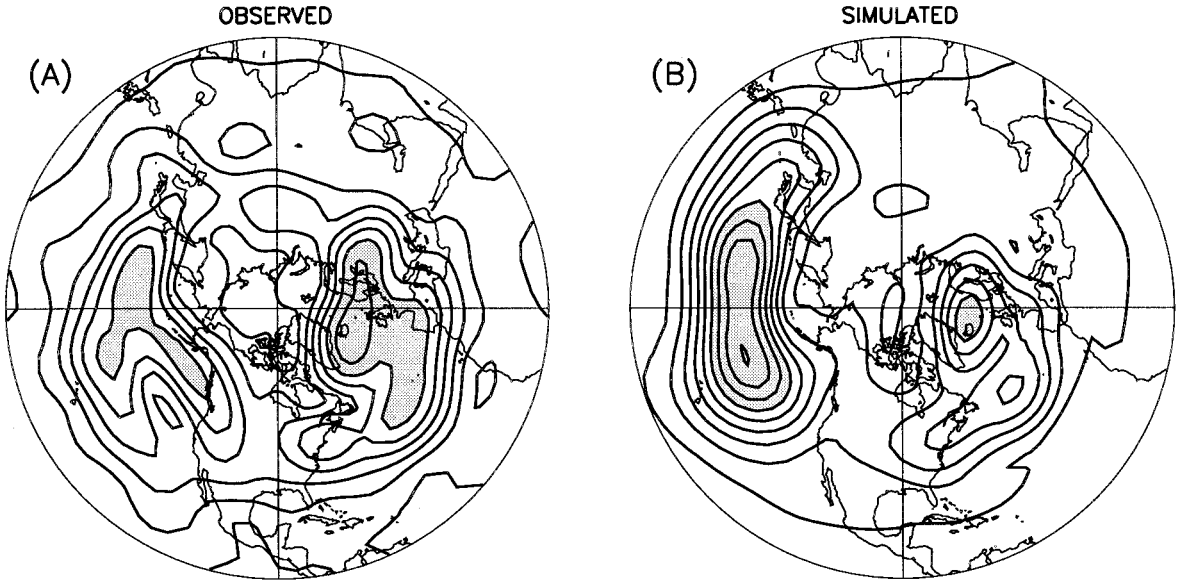

FIG. 12. Observed (a) and simulated (b) standard deviation of DJF mean 400-mb bandpass streamfunction variance for 13 winters (DJF 1982/83–1994/95). Individual winter means were truncated to T12 resolution before standard deviation was computed. Contour interval is 2×10^{12} m^4 s^{-2}; values greater than 1.2×10^{13} m^4 s^{-2} are shaded.

$\mathbf{Q}$ to be white in two other norms; rotational kinetic energy and vorticity. The state variable in the rotational kinetic energy norm is $(1/2)\sqrt{n(n+1)}\Psi_j$, where n is the total wavenumber. The trace of the covariance matrix is then the volume-integrated rotational eddy kinetic energy. The state vector in the vorticity norm is $n(n+1)\Psi_j$. The trace of the covariance matrix is now the volume-integrated eddy enstrophy. As before, the scaling constant ε is chosen so that the maximum rotational eddy kinetic energy of the solution matches observations in each case.

The 400-mb rotational eddy kinetic energy maps for $\mathbf{Q} = \varepsilon\mathbf{I}$ in the rotational kinetic energy and vorticity norms are shown in Figs. 14a and 14b, respectively. The map for $\mathbf{Q} = \varepsilon\mathbf{I}$ in the streamfunction norm was shown in Fig. 2b. The gross features of the solution in the vorticity norm are similar to those in the other two norms, but there are significant differences, which are magnified further when comparing streamfunction variances (not shown). These differences arise mainly because, relative to the streamfunction norm, assuming $\mathbf{Q} = \varepsilon\mathbf{I}$ in the vorticity norm amounts to forcing the larger scales (small n) much more strongly, resulting in a solution that is dominated by planetary-scale low-frequency disturbances. On the other hand, as is clear from comparing Fig. 14a with Fig. 2b, the solutions are nearly identical in the rotational kinetic energy and streamfunction norms. In fact, the solution of the FDR is remarkably insensitive to the norm chosen as long as the largest spatial scales are not forced too strongly relative to the synoptic scales of interest here.

TABLE 1. Summary of results of calculations for individual winter seasons. AC is pattern correlation of observed and simulated T12 anomalous 400-mb bandpass eddy streamfunction variance maps. Anomalies are computed relative to the 13-winter mean. Extra damping included in $\mathbf{D}$ operator for each DJF mean basic state is such that the least damped eigenmode of $\mathbf{B}$ is damped with an e-folding timescale of 20 days. See text for further details.

Winter of	AC
1982/83	0.32
1983/84	0.08
1984/85	−0.25
1985/86	−0.17
1986/87	0.33
1987/88	0.46
1988/89	0.08
1989/90	0.45
1990/91	0.22
1991/92	0.24
1992/93	0.50
1993/94	0.18
1994/95	0.59

There is clearly some arbitrariness in the specification of $\mathbf{Q}$ in (7a), raising the question of which choice is most appropriate. One answer is a $\mathbf{Q}$ that is most consistent with the observed $\mathbf{C}_0$, which may be estimated by specifying $\mathbf{B}$ and $\mathbf{C}_0$ in (5). NSP refer to this as the ''backward'' application of the FDR. Note that the $\mathbf{Q}$ thus obtained is guaranteed to be symmetric, but not positive definite; if so, it may need to be truncated to retain only its positive definite part (see NSP; Penland and Matrosova 1994). We have obtained a truncated positive definite $\mathbf{Q}$ using observed covariances of bandpass-filtered streamfunction at 400 and 800 mb in (5). Before truncation, about 30% of the eigenvalues of $\mathbf{Q}$ were negative, although with magnitudes more than an order of magnitude smaller than the largest positive ei-

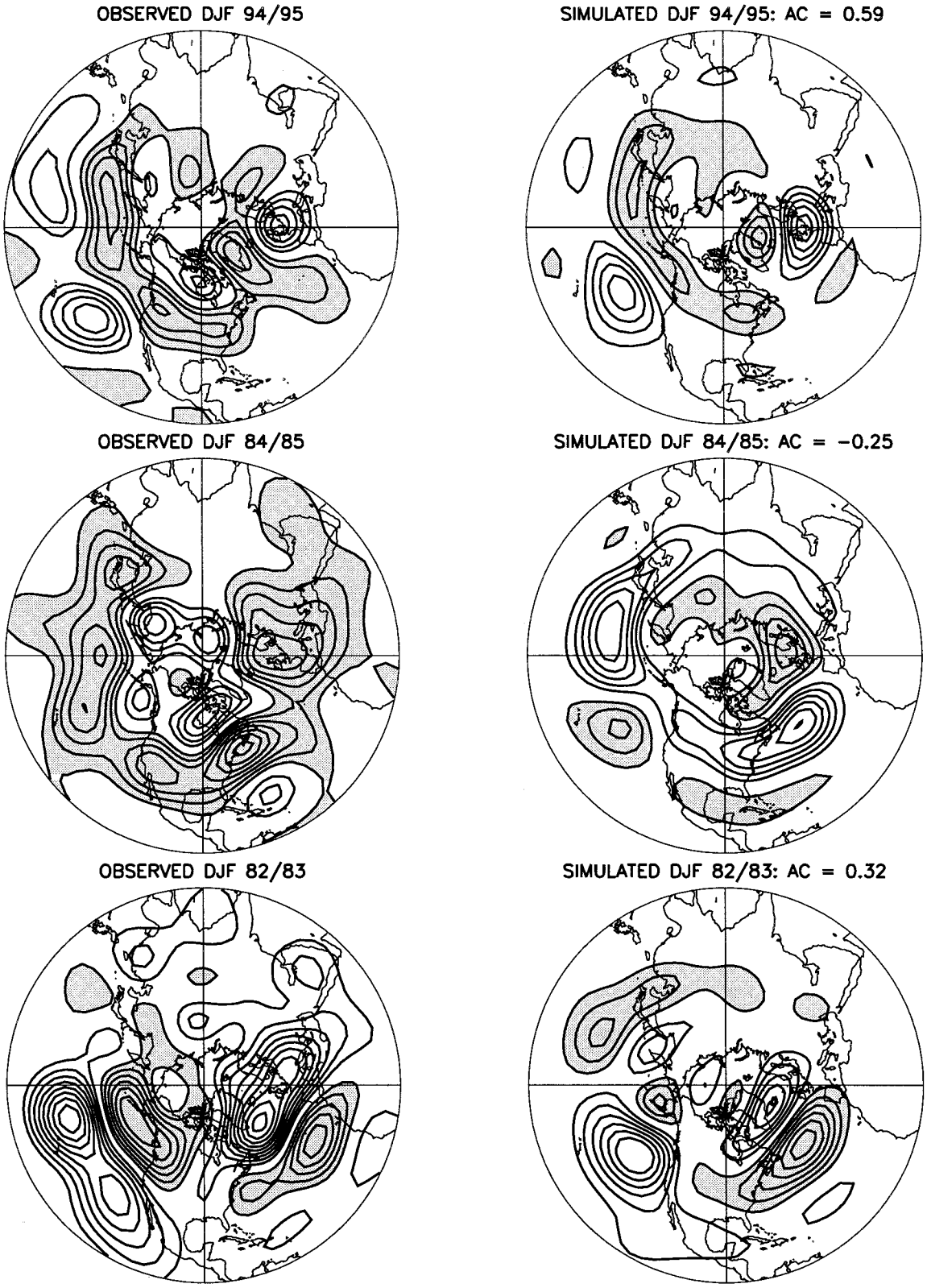

FIG. 13. Observed (left) and simulated (right) anomalous DJF mean 400-mb bandpass streamfunction variance for three selected winters. Fields are truncated to T12 resolution. Contour interval is 3×10^{12} m^4 s^{-2}; values less than -3×10^{12} m^4 s^{-2} are shaded. Anomalies are computed relative to the 13-winter mean (DJF 1982/83–1994/95). Pattern anomaly correlation (AC) between observed and simulated fields is indicated.

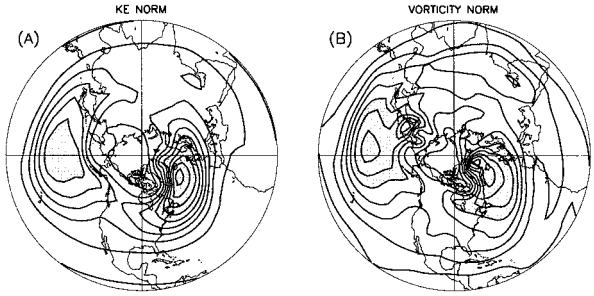

FIG. 14. Simulated DJF mean 400-mb bandpass rotational kinetic energy computed from FDR with stochastic forcing that is spatially white in (a) the kinetic energy and (b) the vorticity norms. Contour interval is 15 $m^2\ s^{-2}$, values greater than 90 $m^2\ s^{-2}$ are shaded.

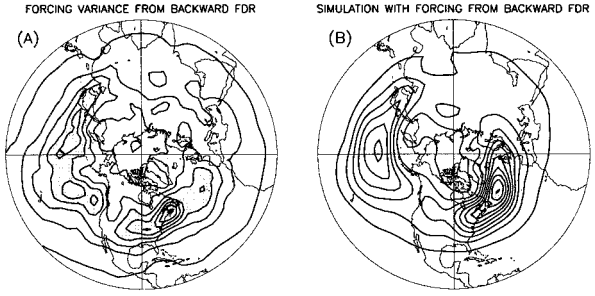

FIG. 15. (a) Map of stochastic forcing variance at 400 mb (the diagonal elements of **Q** displayed in grid space). **Q** computed using observed bandpass streamfunction covariance matrix ($\mathbf{C}_0$) via the backward FDR, and truncated to be positive definite. Contour interval is $2 \times 10^7\ m^4\ s^{-3}$; values greater than $8 \times 10^7\ m^4\ s^{-3}$ are shaded. (b) Streamfunction variance calculated from solution of the FDR using this **Q**. Contour interval is $1 \times 10^{13}\ m^4\ s^{-2}$; values greater than $6 \times 10^{12}\ m^4\ s^{-2}$ are shaded.

genvalues. Figure 15a shows the diagonal elements of the truncated **Q** in grid space. There is some geographical structure to the forcing, especially over North America. If we use this **Q** instead of $\varepsilon\mathbf{I}$ to solve the forward FDR (7a), the $\mathbf{C}_0$ produced (Fig. 15b) is somewhat improved, but otherwise rather similar, to the solution obtained previously (Fig. 1b).[2] The Atlantic storm track is now stronger than the Pacific storm track, in accordance with observations. This is consistent with the region of localized forcing over North America just upstream of the Atlantic storm track (Fig. 15a). Since some knowledge of the observed forcing has been assumed in generating Fig. 15b, the improved agreement of Fig. 15b with Fig. 1a is perhaps not surprising. What is remarkable in our view is the extent to which even Fig. 1b, which was generated without any knowledge of the observed forcing, compares well with Fig. 1a.

b. Sensitivity to **D**

The damping $\mathbf{D} = -\alpha\mathbf{I}$ in (4) must be strong enough to ensure that **B** is stable. In the limit $\alpha \to \infty$, **B** is a diagonal matrix with diagonal elements $-\alpha$, so the FDR yields $\mathbf{C}_0 = \varepsilon\mathbf{I}/(2\alpha)$. Conversely, when α is such that $\lambda_r^{\max} \to 0$, where $\lambda_r^{\max}$ is the damping rate of the least damped mode of **B**, the resulting eddy statistics tend to be dominated by structures nearly identical to those of the phase-quadrature components of the least damped mode of **B**. This may be understood by writing the solution $\mathbf{C}_0$ of the FDR (7) in the form

$$\mathbf{C}_0 = \mathbf{E}\mathbf{H}\mathbf{E}^{\mathrm{T}^*}, \quad \text{with} \quad \mathbf{H}_{ij} = -\frac{[\varepsilon\mathbf{E}^{-1}(\mathbf{E}^{-1})^{\mathrm{T}^*}]_{ij}}{\lambda_i + \lambda_j^*}, \quad (19)$$

where **E** is the matrix of the eigenvectors of **B** (or **L**, since the addition of a linear damping $-\alpha\mathbf{I}$ does not change the eigenvectors) and λ are the eigenvalues of **B** [see appendix C in Penland and Sardeshmukh (1995)].

Now if **B** were normal, the eigenvector matrix **E** would be orthogonal. The trace of $\mathbf{C}_0$ would then be identical to the trace of **H**, which is proportional to the sum of the reciprocals of the real parts of λ. Therefore, in the limit $\lambda_r^{\max} \to 0$, the variance would be dominated by the least damped mode. The argument as stated is not strictly valid if **B** is non-normal, but it is easy to see that in the limit $\lambda_r^{\max} \to 0$, the least damped mode of **B** would dominate the solution (i.e., the two leading eigenvectors of $\mathbf{C}_0$ would have structures nearly identical to those of the phase-quadrature components of the least damped mode of **B**, and together explain most of the variance).

Figure 16 summarizes the sensitivity of the solution to α, expressed in terms of the damping timescale $1/\alpha$. Since **B** is unstable for $1/\alpha > 23.5$ days, only damping timescales in the range of 0–23 days are considered. For $1/\alpha \to 23.5$ days, $\lambda_r^{\max} \to 0$, and as expected from the discussion above, the variance of the solution ($\mathrm{Tr}\mathbf{C}_0$) is large, and the two leading EOFs (eigenvectors of $\mathbf{C}_0$) explain most of the variance. Similar behavior was ob-

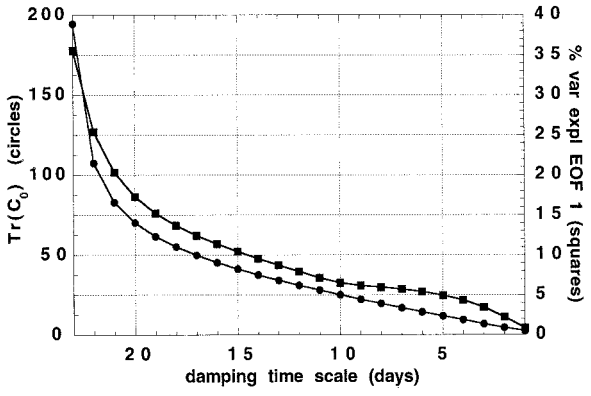

FIG. 16. $\mathrm{Tr}(\mathbf{C}_0)$ (solid circles) and leading eigenvalue of $\mathbf{C}_0$ (solid squares) as a function of damping timescale $1/\alpha$ of the **D** operator. Leading eigenvalue of the covariance matrix expressed as percent variance explained by the first eigenvector. $\mathbf{C}_0$ is calculated by solving the FDR (7a) with the scaling parameter ε chosen so that $\mathrm{Tr}\mathbf{Q} = \mathbf{I}$.

[2] The $\mathbf{C}_0$ computed using the **Q** from the backward FDR is not identical to the observed $\mathbf{C}_0$, because of the truncation that is necessary to make **Q** positive definite.

tained in the study of DelSole and Farrell (1995). As $1/\alpha$ is decreased from 23 days, the fraction of variance explained by the leading eigenvector reduces. For $1/\alpha$ less than 15 days, the leading eigenvector explains less than ten percent of the variance. Therefore, unless α is specified such that the least damped mode of $\mathbf{B}$ is nearly neutral ($\lambda_r^{\max} \to 0$), that least damped mode has no special significance in our solution.

Maps of the diagonal elements of $\mathbf{C}_0$ in grid space—that is, streamfunction variance maps such as Fig. 1b—show some sensitivity to the value of α. For small α, the maps essentially show the amplitude of the least damped mode, which is somewhat higher in the Atlantic storm track than in the Pacific storm track. Given that the structure of the most unstable (or least damped) eigenmodes of non-normal dynamical systems can be sensitive to small variations in model parameters, basic state, and resolution [e.g., see Borges and Sardeshmukh (1995) for a barotropic example] it seems sensible to specify an α large enough that no single structure dominates the solution. For α between 1/20 day^{-1} and 1/5 day^{-1}, the gross characteristics of the solution change little (not shown). There is, however, a tendency for the variance to become more localized in the region of strongest temperature gradients as α is increased. Qualitatively, this means that the simulated Pacific storm track becomes stronger than the Atlantic storm track as α is increased. For large α, the solution essentially becomes a local balance between stochastic forcing and dissipation. The value $\alpha = 1/10$ day^{-1} used in most of our calculations is between these two extremes.

7. Discussion and conclusions

In this paper we have attempted to explain the observed structure of the Northern Hemisphere wintertime synoptic-scale variability, given the structure of the planetary-scale background flow. We have used an extremely simple dynamical model for this purpose. We conjecture that synoptic eddy evolution, *on average*, can be viewed as stochastically forced disturbances evolving on a baroclinically *stable* background flow, so that the eddy statistics are identical to those of the multivariate first-order linear Markov process (4). We then use well-known results from the extensively developed theory of Markov processes to determine those statistics through (7).

To keep the theory simple and as free as possible of arbitrary adjustable parameters, the deterministic part $\mathbf{B}$ of the Markov process is specified to be a linearized two-level quasigeostrophic model $\mathbf{L}$ of extratropical synoptic eddies, plus a uniform damping $\mathbf{D} = -\alpha\mathbf{I}$. The two-level QG model is chosen because it is the simplest model incorporating the basic baroclinic dynamics of extratropical synoptic eddy development; the uniform damping $\mathbf{D}$ because it represents the simplest possible accounting of nonlinear saturation effects. The stochastic forcing part of the Markov model is kept simple by specifying it as geographically incoherent white noise with covariance $\mathbf{Q} = \varepsilon\mathbf{I}$. Our Markov model (4) is thus completely defined by the nondivergent part of the background flow at two levels (400 and 800 mb), three ''standard'' model damping parameters (representing low-level Rayleigh damping, midtropospheric thermal damping, and biharmonic diffusion), one static stability parameter, and α and ε. The value of α actually specified in most of the calculations (1/10 day^{-1}) is small enough to be within the range of uncertainty of the standard model damping parameters, so α need not necessarily be viewed as an additional parameter. Although we did not explore this in detail, we could have obtained similar results by setting α to zero and making minor adjustments to the other damping parameters. In that case, $\mathbf{B}$ would have been identical to $\mathbf{L}$, and the only extra parameter needed to define our Markov model would have been ε. This parameter is essentially a scaling constant, chosen to match observed amplitudes with simulated amplitudes given by a linear theory. It has no effect on the predicted patterns.

It is important to recognize that (4) is only one out of an infinite number of first-order linear Markov models that are applicable to this problem. In particular, we did not determine the dynamical operator $\mathbf{B}$ empirically, as done for example by Penland and Sardeshmukh (1995) and DelSole (1996). These authors determined $\mathbf{B}$ as the solution of (6) with specified observed (or model-generated) covariances $\mathbf{C}_0$ and $\mathbf{C}_\tau$. We also did not determine $\mathbf{D}$ (and thence $\mathbf{B}$) by actually regressing the observed nonlinear and forcing terms against $\tilde{\mathbf{x}}$ in (3). It is possible that $\mathbf{B}$ obtained through either of these approaches would give better results than shown here. However, for an N-dimensional Markov process, we would then have N^2 model parameters in $\mathbf{B}$, instead of the $2 + 4 + N$ (needed to describe the background flow) of our model, and so the ''explaining power'' of such an empirical model would be correspondingly lower. Another very important reason for choosing $\mathbf{B} = \mathbf{L} - \alpha\mathbf{I}$ is that the eigenstructures of $\mathbf{B}$ and $\mathbf{L}$ are the same, and so the deterministic dynamics $\mathbf{B}$ of our model are the well-understood quasigeostrophic dynamics of synoptic eddies. The only difference is that the eddies are now damped.

Despite these drastic simplifications, our model performs well. It simulates most of the major features of the wintertime climatological storm tracks such as the geographical distributions and intensities of the eddy variances, lagged covariances, rotational kinetic energy, and vorticity and heat fluxes (Figs. 1–5). It simulates not only the aggregate statistics of the eddies as revealed in these measures, but also the statistical structure of the eddies themselves (Figs. 6–7). Indeed (4) used as a forecast model for the individual observed eddies easily outperforms a persistence forecast model (Figs. 9–10). The model is also able to simulate correctly the change in the relative strengths of the Pacific and Atlantic storm tracks from January to April (Fig. 11), and is able to

capture some of the interannual variability of the wintertime storm tracks (Fig. 12). We stress again that it is able to do all this given only the planetary-scale background flow plus a few damping and scaling parameters. The results are relatively insensitive to the values of those damping parameters, except when they are such that the least damped mode of **B** is almost neutral (Fig 16). They are also relatively insensitive to the specification of the space in which the stochastic forcing is assumed to be white, as long as the forcing does not excite the largest planetary scales of the flow much more strongly than other scales.

Even a cursory comparison of Figs. 1a and 1b suggests the power of this simple theory. The idea that synoptic eddies behave on average as stochastically forced eddies evolving on a baroclinically stable background flow clearly goes a long way toward explaining the general structure of observed storm tracks. In our model the eddies are being forced uniformly everywhere on the hemisphere, on all scales. The reason they grow near the Pacific and Atlantic jets into recognizable weather systems is that they can efficiently draw upon the potential (and to a lesser extent, the kinetic) energy available in those jets (Fig. 8). *No exponential instability* needs to be invoked. As discussed in the introduction, this is entirely consistent with the view of Farrell and his collaborators.

Whether the climatological mean state of the atmosphere is actually exponentially unstable, and whether such instability is important for synoptic-scale tropospheric motions, are in our view still open questions. The most unstable eigenmode of the climatological DJF mean flow is only weakly unstable in our model, with an *e*-folding timescale of 23.5 days. We believe this to be more a result of the relative smoothness of that flow than of our particular choice of dissipation constants. Hall and Sardeshmukh (1998) have recently investigated the stability of the observed long-term mean northern winter flow in a T31, 10-level primitive equation model, and found that it is stable for an average damping timescale of 1 day in the layer 1000–800 mb. This is consistent with the 2.5-day Rayleigh damping specified in the lower half, and no or weak damping in the upper half, of our T31, two-level QG model. The 2.5-day damping is also consistent with the range of observed values and with theoretical considerations of Ekman-layer dynamics. The momentum budget study of Klinker and Sardeshmukh (1992) suggests a damping timescale of about 5 days for the column average, that is, about 2.5 days for the lower half of the atmosphere. Energy budget studies such as that of Peixoto and Oort (1992, their Table 14.1) suggest a kinetic energy damping timescale of 3.5 days in the wintertime Northern Hemisphere as a whole. This is a gross number, but is perhaps reliable and interesting for that very reason. One may translate it into a column-average momentum damping timescale of 7 days over the hemisphere, not inconsistent with the 5 days found by Klinker and Sardeshmukh in midlatitudes. The theoretical considerations of Pierrehumbert and Swanson (1995, p. 425) suggest that if boundary layer friction is represented as a Rayleigh drag applied over a depth D (say 2 km), the appropriate damping timescale to specify should be approximately $\tau = D/(f_0\delta_e)$, where δ_e is the Ekman depth ($\sim$200 m) and f_0 is the Coriolis parameter. According to this, τ should be about 1 day for the 1000–800-mb layer in midlatitudes, which again translates into 2.5 days for the layer 1000–500 mb.

The extra 10-day damping α in our model is relatively weak. Note that even if one views it as a crude representation of neglected nonlinear terms, those nonlinear terms need not be associated with the nonlinear saturation of exponential instability. Eddies growing through stable interactions with the mean flow (as in Fig. 8) could certainly reach large amplitude and evolve nonlinearly thereafter, an effect that is not included in our linear **L** operator.

In any event, regardless of the baroclinic instability or otherwise of the long-term mean flow, our results show that it is not necessary to invoke it in order to model the statistics of observed synoptic eddies. The energy balance in our model is between the stochastic forcing and stable baroclinic and barotropic energy extraction from the sheared flow on the one hand, and eddy dissipation on the other. As suggested by Fig. 1, of the three energy sources available to the eddies, they draw most heavily upon the available potential energy source. The stochastic source is of secondary importance.

It is interesting to contrast our results with those of DelSole (1996). He attempted to fit a Markov model to the variability simulated in a two-layer nonlinear quasigeostrophic channel model with zonally symmetric forcing and boundary conditions, but had mixed results. Given that he was only attempting to explain the variability of his two-layer model and not of the observed atmosphere as we have done, his aim was less ambitious, and therefore his relative lack of success all the more puzzling. One possible explanation is that we have considered zonally varying background states, and he did not. Eddies growing in our model can leave the baroclinically active regions and decay by barotropic processes as shown in Figs. 6 and 7. In DelSole's model, eddies grow on a zonally symmetric basic state and are confined to a reentrant channel, and hence never enter a region unfavorable for eddy growth. Nonlinear processes may then be considerably more important in halting the growth of eddies in his model. Another difference is that DelSole was trying to explain all of the variability in his model, not just synoptic-scale variability.

Our model has some notable deficiencies. It does not simulate the northeastward extension of the wintertime Pacific storm track into North America (Fig. 1). In general it produces too strongly tilted eddies in the Pacific and Atlantic storm tracks (Figs. 6–7), and thus too

strong vorticity fluxes (Fig. 3). It also does not capture the midwinter minimum of the Pacific storm track. And finally, although it is able to simulate the anomalous storm tracks of some individual winters (such as DJF 1994/95, see Fig. 13), its general skill is poor in this regard (Table 1).

Some of these failures, especially the poor simulation of the eastern edge of both the climatological Pacific storm track (Fig. 1) and its interannual variability (Fig. 13), are probably due to the simplicity of our two-level quasigeostrophic **L** operator. The inability of the model to capture the Pacific midwinter minimum may also reflect inadequacies of **L**. It would certainly be worthwhile to repeat these calculations with a multilevel primitive equation model to see if these deficiencies can be remedied.

It is important to remember, however, that our model does not consist of **L** alone, but also of **D** and **Q**; and low-frequency variations of the storm tracks may also be associated with low-frequency variability of **D** and **Q**. We have stressed that their detailed specification is secondary, indeed that they may be characterized by just two constants α and ε. Incorporating more complicated formulations of **D** and **Q** could lead to better simulations of the annual and interannual variability of the storm tracks. Lacking any theoretical guidance in this direction, however, we prefer to leave **D** and **Q** as simple as possible. In section 5b, we allowed α to be flow dependent in an attempt to simulate the interannual variability of the storm tracks. This was done to avoid the resonant behavior of the FDR when **B** is almost exactly neutral. We could have circumvented this problem by choosing a larger α, say 1/7 day^{-1}. Instead, we chose α such that the least damped mode of **B** always decayed with a timescale of 20 days. Calculations for the three winters shown in Fig. 13, when repeated with α fixed at 1/7 day^{-1}, gave very similar results (not shown). This suggests that the simulated interannual variations of the storm tracks (Figs. 12 and 13) are associated mainly with variations of **L**, not of **D** or **Q**.

It is interesting that the model (7) can capture so much of the interannual variability of the storm tracks by invoking only interannual changes of **B** but not of **Q**—that is, by assuming that the symmetric part of $\mathbf{BC}_0$ remains the same from year to year. This suggests an adjustment between the mean flow (represented in **B**) and the synoptic eddy statistics (represented in $\mathbf{C}_0$) on interannual timescales, which could be viewed as perhaps the broadest possible manifestation of an ''index cycle'' in the atmosphere. Even so, the simulations in Fig. 13 are clearly far from perfect. The poor correlations in Table 1 further drive home the point that there is much more to the interannual variability of storm tracks than a simple generalized index cycle. Perhaps the variations of **Q**, which certainly exist, cannot be ignored in even the simplest theory. As suggested by Fig. 11, specifying some variation in the magnitude of **Q** would help us simulate the Pacific midwinter minimum better. We have not pursued such variations here because we do not have any dynamical theory of them.

Notwithstanding the caveats concerning the simplicity of our **B** operator and the simplicity and constancy of our **Q** operator, we believe, for reasons discussed in section 2, that the failure of our model to simulate the anomalous storm tracks for individual winters points to a more fundamental problem: that a significant part of the interannual variability of seasonal-mean storm tracks is not parameterizable in terms of seasonal-mean flow anomalies. To that extent, we believe that repeating our calculations with bigger and better **L** operators might lead to diminishing returns, given the already reasonably good results reported here.

In summary, we have presented a simple model of extratropical storm tracks in which the storm tracks arise from stochastically forced disturbances reaching relatively large amplitudes in certain preferred regions of the atmosphere through *stable* energy interactions with the local background flow. The model successfully explains many observed aspects of the climatological wintertime Pacific and Atlantic storm tracks. It is also successful in explaining some aspects of their annual cycle and interannual variability. It can sometimes predict the anomalous storm tracks for individual seasons; its general ability is however poor in this regard. This failure could be viewed as exposing the inadequacies of the theory. Alternatively, it could be viewed as highlighting the existence of a portion of the seasonal storm-track variability that is unrelated to that of the seasonal flow, and is therefore unparameterizable in terms of the seasonal flow.

Acknowledgments. Support for this research was provided through the NOAA Office of Global Programs. It is a pleasure to thank Dr. Cécile Penland for generously sharing her knowledge of stochastic processes and modeling, and Dr. Matthew Newman for helping to streamline the calculations performed here. The thoughtful and thought-provoking comments of three anonymous reviewers are also greatly appreciated.

REFERENCES

Arnold, L., 1974: *Stochastic Differential Equations: Theory and Applications.* Wiley and Sons, 228 pp.

Blackmon, M. L., J. M. Wallace, N.-C. Lau, and S. L. Mullen, 1977: An observational study of the Northern Hemisphere wintertime circulation. *J. Atmos. Sci.,* **34,** 1040–1053.

Borges, M. D., and P. D. Sardeshmukh, 1995: Barotropic Rossby wave dynamics of zonally varying upper-level flows during northern winter. *J. Atmos. Sci.,* **52,** 3779–3796.

Branstator, G., 1995: Organization of stormtrack anomalies by recurring low-frequency circulation anomalies. *J. Atmos. Sci.,* **52,** 207–226.

DelSole, T., 1996: Can quasi-geostrophic turbulence be modeled stochastically? *J. Atmos. Sci.,* **53,** 1617–1633.

——, and B. F. Farrell, 1995: A stochastically excited linear system as a model for quasigeostrophic turbulence: Analytic results for one- and two-layer fluids. *J. Atmos. Sci.,* **52,** 2531–2547.

Farrell, B. F., 1989: Optimal excitation of baroclinic waves. *J. Atmos. Sci.,* **46,** 1193–1206.
——, and P. J. Iannou, 1993: Stochastic dynamics of baroclinic waves. *J. Atmos. Sci.,* **50,** 4044–4057.
——, and ——, 1994: A theory for the statistical equilibrium energy and heat flux produced by transient baroclinic waves. *J. Atmos. Sci.,* **51,** 2685–2698.
——, and ——, 1995: Stochastic dynamics of the midlatitude atmospheric jet. *J. Atmos. Sci.,* **52,** 1642–1656.
Frederiksen, J. S., 1983: Disturbances and eddy fluxes in Northern Hemisphere flows: Instability of three-dimensional January and July flows. *J. Atmos. Sci.,* **40,** 836–855.
——, 1989: The role of instability during the onset of blocking and cyclogenesis in Northern Hemisphere synoptic flows. *J. Atmos. Sci.,* **46,** 1076–1092.
Gardiner, C. W., 1985: *Handbook of Stochastic Methods for Physics, Chemistry and the Natural Sciences.* Springer-Verlag, 442 pp.
Green, J. S. A., 1977: The weather during July 1967: Some dynamical considerations of the drought. *Weather,* **32,** 120–128.
Hall, N. M. J., and P. D. Sardeshmukh, 1998: Is the time-mean Northern Hemisphere flow baroclinically unstable? *J. Atmos. Sci.,* **55,** 41–58.
Held, I. M., S. W. Lyons, and S. Nigam, 1989: Transients and the extratropical response to El Niño. *J. Atmos. Sci.,* **46,** 163–174.
Hoerling, M. P., and M. Ting, 1994: Organization of extratropical transients during El Niño. *J. Climate,* **7,** 745–766.
Hoskins, B. J., and P. D. Sardeshmukh, 1987a: Transient eddies and the seasonal mean rotational flow. *J. Atmos. Sci.,* **44,** 328–338.
——, and ——, 1987b: A diagnostic study of the dynamics of the Northern Hemisphere winter of 1985–86. *Quart. J. Roy. Meteor. Soc.,* **113,** 759–778.
——, I. N. James, and G. H. White, 1983: The shape, propagation and mean-flow interaction of large-scale weather systems. *J. Atmos. Sci.,* **40,** 1595–1612.
Kalnay, E., M. Kanamitsu, R. Kistler, W. Collins, D. Deaven, L. Gandin, M. Iredell, S.-Saha, G. White, J. Woollen. Y. Zhu, M. Chelliah, W. Ebisuzaki, W. Higgins, J.-Janowiak, K. C. Mo, C. Ropelewski, J. Wang, A. Leetma, R. Reynolds, R. Jenne, and D. Joseph, 1996: The NCEP/NCAR 40-Year Reanalysis Project. *Bull. Amer. Meteor. Soc.,* **77,** 437–471.
Klinker, E., and P. D. Sardeshmukh, 1992: The diagnosis of mechanical dissipation in the atmosphere from large-scale balance requirements. *J. Atmos. Sci.,* **49,** 608–627.
Kok, C. J., and J. D. Opsteegh, 1985: On the possible causes of anomalies in seasonal mean circulation patterns during the 1982–83 El Niño event. *J. Atmos. Sci.,* **42,** 677–694.
Kraichnan, R. H., 1959: The structure of isotropic turbulence at very high Reynolds numbers. *J. Fluid Mech.,* **5,** 497–543.
Lau, N.-C., 1988: Variability of the observed midlatitude storm tracks in relation to low-frequency changes in the circulation pattern. *J. Atmos. Sci.,* **45,** 2718–2743.
——, and E. O. Holopainen, 1984: Transient eddy forcing of the time-mean flow as identified by geopotential tendencies. *J. Atmos. Sci.,* **41,** 313–328.
Leith, C., 1971: Atmospheric predictability and two-dimensional turbulence. *J. Atmos. Sci.,* **28,** 145–161.
Lorenz, E., 1960: Energy and numerical weather prediction. *Tellus,* **4,** 364–373.
Metz, W., 1989: Low-frequency anomalies of atmospheric flow and the effect of cyclone scale eddies: A canonical correlation analysis. *J. Atmos. Sci.,* **46,** 1026–1041.
Nakamura, H., 1992: Midwinter suppression of baroclinic wave activity in the Pacific. *J. Atmos. Sci.,* **49,** 1629–1642.
——, and J. M. Wallace, 1990: Observed changes in baroclinic wave activity during the life cycles of low-frequency circulation anomalies. *J. Atmos. Sci.,* **47,** 1100–1116.
Newman, M., P. D. Sardeshmukh, and C. Penland, 1997: Stochastic forcing of the wintertime extratropical flow. *J. Atmos. Sci.,* **54,** 435–455.
Peixoto, J. P., and A. Oort, 1992: *Physics of Climate.* American Institute of Physics, 520 pp.
Penland, C., 1989: Random forcing and forecasting using principal oscillation pattern analysis. *Mon. Wea. Rev.,* **117,** 2165–2185.
——, and M. Ghil, 1993: Forecasting Northern Hemisphere 700-mb geopotential heights using principal oscillation patterns. *Mon. Wea. Rev.,* **121,** 2355–2372.
——, and L. Matrosova, 1994: A balance condition for stochastic numerical models with applications to the El Niño–Southern Oscillation. *J. Atmos. Sci.,* **51,** 207–226.
——, and P. D. Sardeshmukh, 1995: The optimal growth of sea surface temperature anomalies. *J. Climate,* **8,** 1999–2024.
Pierrehumbert, R. T., and K. L. Swanson, 1995: Baroclinic Instability. *Annu. Rev. Fluid Mech.,* **27,** 419–467.
Robertson, A. W., and W. Metz, 1989: Three-dimensional linear instability of persistent anomalous large-scale flows. *J. Atmos. Sci.,* **46,** 2783–2801
——, and ——, 1990: Transient-eddy feedbacks derived from linear theory and observations. *J. Atmos. Sci.,* **47,** 2743–2764.
Sardeshmukh, P. D., M. Newman, and M. D. Borges, 1997: Free Rossby wave dynamics of the wintertime low-frequency flow. *J. Atmos. Sci.,* **54,** 5–23.
Valdes, P. J., and B. J. Hoskins, 1989: Linear stationary wave simulations of the time mean climatological flow. *J. Atmos. Sci.,* **46,** 2509–2527.
Wallace, J. M., G.-H. Lim, and M. Blackmon, 1988: Relationship between cyclone tracks, anticyclone tracks and baroclinic waveguides. *J. Atmos. Sci.,* **45,** 439–462.